

Light-atom coupling with 4Pi Microscopy

Chin Yue Sum

Centre for Quantum Technologies
National University of Singapore

A thesis submitted for the degree of
Doctor of Philosophy

Supervisor:

Professor Christian Kurtsiefer

Examiners:

President's Assistant Professor Huanqian Loh

Professor Síle Nic Chormaic

Professor Mark Saffman

July 2018

Declaration

I hereby declare that this thesis is my original work and it has been written by me in its entirety. I have duly acknowledged all the sources of information which have been used in the thesis. This thesis has also not been submitted for any degree in any university previously.



Chin Yue Sum
July 2018

Acknowledgements

The day I joined the Quantum Optics group dates back to 2011 as an undergraduate. Shamelessly knocking on Christian's door, I asked if there were anything to work on during the summer. His response was absolutely heartwarming, without hesitation, toured me around the lab, reckoned that we will figure something out, and so here I am on this journey. I express my gratitude to him for the full liberty to learn, explore, experiment, and also the opportunity to work with all the wonderful members of this group.

The fruit of this thesis is to be shared with my mentor, Matthias Steiner, for contributing in every aspect to this experiment since the conception, from drafting plans to turning mirrors. Not to discount also the constant flow of ideas, discussion, and physical insights coming from you. We've had our ups and downs and I certainly could not have wished for a better mentor. Thank you.

Heartfelt appreciation to 'guru' Victor, the predecessor of this experiment, for polishing and leaving us a set of data processing tools that are accessible by non-gurus. Your awesome programming skills and one liner hacks have been a great improvement to our quality of life. I would also like to thank Nick for aiding with the vacuum system and mechanical parts.

Special thanks to Gleb, for patiently introducing me to experimental physics. It must have been troublesome to explain every little thing when I was completely fresh. Further thanks to Alessandro, for the subsequent guidance especially on organization and presentation. I too appreciate the insightful discussion from Chi Huan, as much as a peer, you were too a teacher to me. Remaining big thanks goes to all the other members of the Quantum Optics group, including Brenda, Hou Shun, Peng Kian, Yicheng, Jianwei, Lijiong, Mathias Seidler, Adrian, and Janet. All of you have definitely contributed to this journey in one way or other.

Finally thanks to the kind support from my friends and family, which has provided me the strength and endurance for this journey.

Abstract

An efficient light-matter interface is foundational to the development of a distributed quantum network. In this thesis, we explore the possibility of an efficient light-atom interface in free space. Our approach utilises a pair of high numerical aperture (NA=0.75) lenses to tightly focus light onto single ^{87}Rb atoms. Operating near the diffraction limit, the length scale of the light field approaches that of the thermal motion of trapped atoms. Therefore, we focus on our studies not only on the localisation of the light field but also of the atoms.

First, we investigate polarization gradient cooling of single atoms in optical dipole traps to reduce the thermal motion. We then quantify the effect of residual thermal motion on our light-atom interface with a transmission spectroscopy experiment. Comparing the results to a simple model, we deduce that the residual thermal motion reduces the interaction by less than 10%. The findings from these experiments lay down the foundations for this thesis.

In the main experiment, we adapt a super-resolution imaging technique, 4Pi microscopy, to elevate the focusing limit of our system. In this configuration, the light field is split and coherently focused onto the atom by two opposing lenses. We demonstrate 36.6(3)% extinction of the incident field, which is the largest value reported for an atomic emitter in free space. Such a large extinction leads to significant nonlinear light-atom interaction observed as modified photon statistics of the transmitted field. Our results pave the way towards deterministic photon absorption by the atom with a free-space approach.

Table of contents

1	Introduction	1
2	Experimental setup and manipulation of single atoms	5
2.1	Setup overview	5
2.2	Aspheric lens pair	5
2.2.1	Mechanical mount	6
2.2.2	Light-atom interaction strength	7
2.2.3	Preliminary test	8
2.3	Vacuum system	9
2.4	Laser system	10
2.5	Magneto-Optical Trap (MOT)	12
2.5.1	MOT beams	13
2.5.2	Magnetic quadrupole field	13
2.6	Far-off-resonant optical dipole trap	14
2.6.1	Implementation	15
2.6.2	Characterisation	16
2.6.3	Trapping lifetime	16
2.7	Manipulation of single atoms	19
2.7.1	State-selective detection	19
2.7.2	Optical pumping	20
3	Polarization gradient cooling in optical dipole traps	23
3.1	Introduction	23
3.1.1	Effect of light shifts on PGC	24
3.1.2	One-dimensional PGC semi-classical simulation	25
3.2	Experimental realisation	28
3.2.1	Optical setup	28
3.2.2	Temperature measurement	29

3.3	PGC dependence on trap polarization	32
3.3.1	Linearly and circularly polarized trap	32
3.3.2	Imperfect linearly polarized trap	33
3.3.3	Switching trap polarization after PGC	34
3.4	Summary	35
4	Quantifying free-space light-atom interaction	36
4.1	Transmission measurement	36
4.1.1	Basic idea	36
4.1.2	Experimental realisation	38
4.1.3	Results	40
4.2	Saturation measurement	41
4.2.1	Basic idea	41
4.2.2	Experimental realisation	42
4.2.3	Results	43
4.3	Role of thermal motion on interaction	45
4.3.1	Model	46
4.3.2	Results	47
4.4	Summary	49
5	Nonlinear photon-atom coupling with 4Pi microscopy	51
5.1	Introduction	51
5.1.1	Transmission measurement in 4Pi configuration	52
5.1.2	Numerical simulation of electric field distribution	54
5.2	Experimental realisation	56
5.2.1	Optical setup	56
5.2.2	Experimental sequence	57
5.2.3	Active phase stabilisation	57
5.2.4	Postselection of the atom position	58
5.3	Transmission experiment	60
5.3.1	Comparison between 4Pi and one-sided illumination	60
5.3.2	4Pi illumination coupling dependence on power splitting	62
5.4	Observation of nonlinear light-atom coupling	64
5.4.1	Photon statistics of transmitted light	64
5.4.2	Measurement of second-order correlation function	64
5.4.3	Results and analysis	66
5.5	Summary	67

Table of contents

6 Conclusion and Outlook	68
Appendix A List of Publications and Conferences	70
References	71

Chapter 1

Introduction

The study of light-atom interaction has been driven by the progress and promising applications of quantum information science, for instance, quantum computing, quantum communication, and metrology. In this context, both light and atom play the role of a quantum bit (qubit), which is the basic unit of quantum information [1]. Distinct from its classical counterpart with well defined logical states of 0 and 1, the qubit can be either 0 or 1, or any coherent superposition of the two. Furthermore, multiple qubits can be entangled, for which each qubit cannot be wholly described individually. These properties enable algorithms that reduce the computational complexity of problems, for example, factorisation of large numbers with Shor's algorithm [2] and database search with Grover's algorithm [3]. Already, pioneering research has demonstrated respective proof-of-principle experiments [4–7].

For quantum algorithms to practically outperform their classical counterparts, scaling up quantum systems is inevitable [8, 9]. Recent developments focus on increasing locally the number of qubits using superconducting qubits [10], atomic arrays [11, 12], and trapped ions [13, 14]. While local computing power is essential, the next important step is to improve connectivity between different quantum systems to exchange quantum information over large physical distances. Such connectivity not only enables quantum communication protocols but also lifts the physical scaling limitation of a single quantum system. A notional method to achieve quantum connectivity is to construct a distributed quantum network which consists of: (1) stationary qubits, formed by atoms (or other quantum emitters) to process and store quantum information, and (2) flying qubits, formed by photons to transfer quantum information between the stationary nodes [15–17]. A major challenge lies in increasing the interaction strength of the atoms with incoming photons. This is

the key ingredient for efficient exchange of quantum information between atoms and photons.

Currently, various efforts are underway to develop suitable building blocks for a quantum network with different quantum emitters such as single neutral atoms [18, 19], atomic ensembles [20], Rydberg atoms [21, 22], trapped ions [23, 24], quantum dots [25], and colour centres in diamonds [26]. Among the numerous quantum emitters, single trapped atoms are a particularly good experimental platform for quantitative comparison of light-matter experiments with quantum optics theory. The relative simplicity of single atoms, along with the unperturbed energy level structure and isolation in ultra-high vacuum permits deriving the interaction strength with a minimum of assumptions.

Free-space light-matter interface

There are a few approaches to increase the interaction strength between light and a single atom. The first utilises cavity quantum electrodynamics (QED) effects to enhance the strength of the light field and achieve deterministic photon absorption by the atom [27–29, 19]. An alternative approach is based on tightly focusing a light field onto the atom in free space. The free-space approach is more robust as it does not require precise active stabilisation of the cavity length to operate. The practical relevance of this technological simplicity offers upward scalability when combined with progressive methods in trapping many individual atoms [11, 12]. Fundamentally, it also offers a possibility of studies involving continuum dynamics (as opposed to a cavity-QED system with a discrete mode spectrum) [30, 31]. Recent technological advancement in engineering various waveguide structures to tightly confine the light field also demonstrated the feasibility of near-deterministic coupling [32–35].

The development of effective focusing schemes is a long-standing theoretical [36–40] and experimental challenge. While ongoing research explores focusing techniques with multi-element objectives [41–45], singlet [46, 47] and Fresnel lenses [48], and parabolic mirrors [49, 50], it remains an open question whether near-deterministic absorption of single photons is experimentally possible. The interaction strengths observed with these configurations [39, 51] have fallen short of their theoretically expected capabilities. Aside from imperfections of the focusing devices, the finite positional spread of the single atomic emitter is commonly suspected to reduce the interaction [52]. Consequently, a better understanding of the underlying reasons is necessary to further improve the interaction strength.

We choose to follow a conceptually simple approach of focusing light onto single atoms with a lens. Early efforts in our group used a lens with a numerical aperture $NA=0.55$, which demonstrated 9.8% extinction [46] and 1° phase shift [53] of a weak coherent field. Subsequent work further investigated the excitation probability of an atom depending on the temporal profile of the photons [54, 47]. In this thesis, we employ a larger numerical aperture lens with $NA=0.75$ and seek to experimentally answer the following questions:

- Does tighter focusing lead to stronger light-atom interaction?
- How does the thermal motion of a trapped atom affect the interaction?
- How to achieve stronger light-atom interaction with existing lenses?

The first two posed questions are coupled. Ideally, at tighter focusing we expect a stronger light-atom interaction. However, simultaneously at tighter focusing, the thermal motion of the atom is expected to reduce the interaction. To answer the third question, we borrow an idea from the imaging community.

Inspiration from high-resolution imaging

From high-resolution imaging, it is well-known that a small focal volume requires optical elements which cover a large fraction of the solid angle [55]. While standard confocal optical microscopy already accomplished very small probe volumes, the excitation light is focused through a lens that can cover only up to half of the solid angle, limiting the axial resolution due to a focal volume elongated along the optical axis. This limitation has been overcome by a super-resolution technique, known as 4Pi microscopy [56, 57], which utilises two opposing lenses with a common focus. In this configuration the incident beam is split, and the object is coherently illuminated by two counter-propagating parts of the field. Similarity between imaging and excitation of a quantum emitter suggests that a 4Pi arrangement can also be used to efficiently couple light to an atom. To this end, we dedicate the later part of this thesis to the implementation of a light-atom interface based on 4Pi microscopy.

Thesis outline

This thesis is organised as follows:

- Chapter 2 outlines the foundation of the experimental setup where we briefly summarise each component of the apparatus. The details of trapping and

manipulating single atoms are provided along with some calibration measurements.

- Chapter 3 reports on our experimental efforts on polarization gradient cooling (PGC) of single atoms in optical dipole traps [58]. We explore the differences in minimum achievable temperatures in a linearly polarized and a circularly polarized trap. Demonstrating that switching the trap polarization from linear to circular after PGC induces only minor heating, we subsequently use this method for our experiments detailed in Chapter 4 and 5.
- Chapter 4 describes the characterisation of the light-atom coupling efficiency of our system with two approaches: a transmission extinction measurement and a saturation measurement [59]. We further quantify the effect of atomic thermal motion on the interaction.
- Chapter 5 presents the implementation of a light-atom interface based on a super-resolution technique, known as 4Pi microscopy [60]. We show that the interaction strength is doubled compared to one-sided illumination that was first presented in Chapter 4. Our observation of modified photon statistics of the transmitted field furthermore indicates nonlinear interaction at the single-photon level.
- Chapter 6 summarises our findings and provides an outlook for future directions.

Chapter 2

Experimental setup and manipulation of single atoms

This chapter introduces the experimental setup and techniques to trap single ^{87}Rb atoms. We briefly present each key component: the aspheric lens pair, the vacuum system, the laser system, the MOT, and the FORT. We then describe the manipulation of single atoms, which includes state-selective detection and optical pumping.

2.1 Setup overview

Figure 2.1 shows the schematic of our optical setup. We hold a single ^{87}Rb atom with a far-off-resonant optical dipole trap (FORT) operating at a wavelength of 851 nm at the joint focus of an aspheric lens pair. To load atoms into the FORT, we start with a cloud of laser cooled atoms in a magneto-optical-trap (MOT). The fluorescence light scattered by the atom is collected with the aspheric lens pair, coupled into single mode fibres, and then detected via avalanche photodetectors.

2.2 Aspheric lens pair

The core of the optical setup is a pair of high numerical aperture (NA) aspheric lenses. We employ these lenses primarily to tightly focus light onto a single atom to achieve efficient coupling. The previous iteration of this experiment used off-the-shelf moulded glass aspheric lenses (350230-B) with NA=0.55 by LightPath Technologies [61–63]. To attain aspheric lenses with higher NA, we opt for a custom design by Asphericon, tailored with the following properties:

2.2. Aspheric lens pair

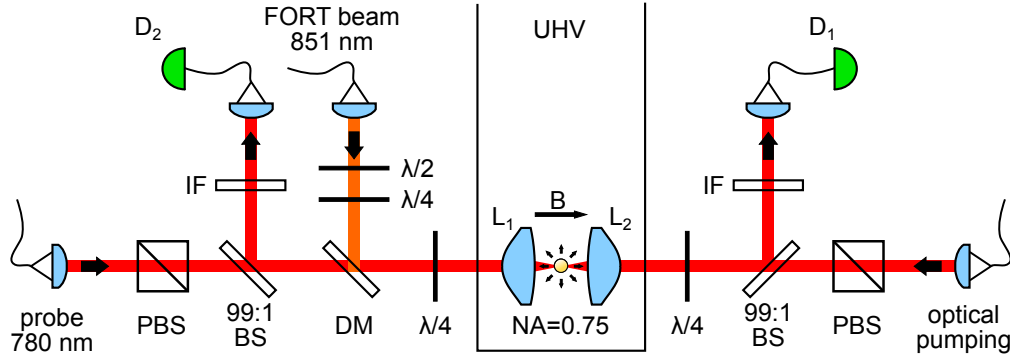


Fig. 2.1 Optical setup for probing light-atom interaction in free space. A single atom is held at the joint focus of two high NA lenses (L_1 , L_2) using a far-off-resonant optical dipole trap (FORT) within an ultra-high vacuum (UHV) chamber. The lenses are also used to focus probe light onto the atom and to collect fluorescence light scattered by the atom. D_1 , D_2 : avalanche photodetectors (APDs), IF: interference filter centred at 780 nm, $\lambda/2$: half-wave plate, $\lambda/4$: quarter-wave plate, (P)BS: (polarizing) beam splitter, DM: dichroic mirror, \mathbf{B} : magnetic field.

- numerical aperture: 0.75
- effective focal length: 5.95 mm
- clear aperture: 13.5 mm
- back focal length: 3.16 mm
- design wavelength: 780 nm
- anti-reflection coating: $< 0.5\%$ at 700-1400 nm
- material: S-LAH79 ($n_d = 2.0033$)

On top of that, the lenses are designed and tested to perform at the diffraction limit with a root-mean-square (RMS) wavefront error $\sigma < 0.070\lambda$ by the manufacturer.

We choose to use aspheric lenses over multi-element microscope objectives for their compactness and lower cost. The compact size of an aspheric lens allows a lens pair to be fitted into a small cuvette which greatly simplifies the vacuum system.

2.2.1 Mechanical mount

Figure 2.2 shows the lens pair mounted on an aluminium holder. The aluminium holder consists of a main frame and two detachable lens mounts. The lens mounts are not made equal such that one fits on the aluminium holder while the other is smaller to allow for fine adjustment. Outside the vacuum chamber, we position the lens pair

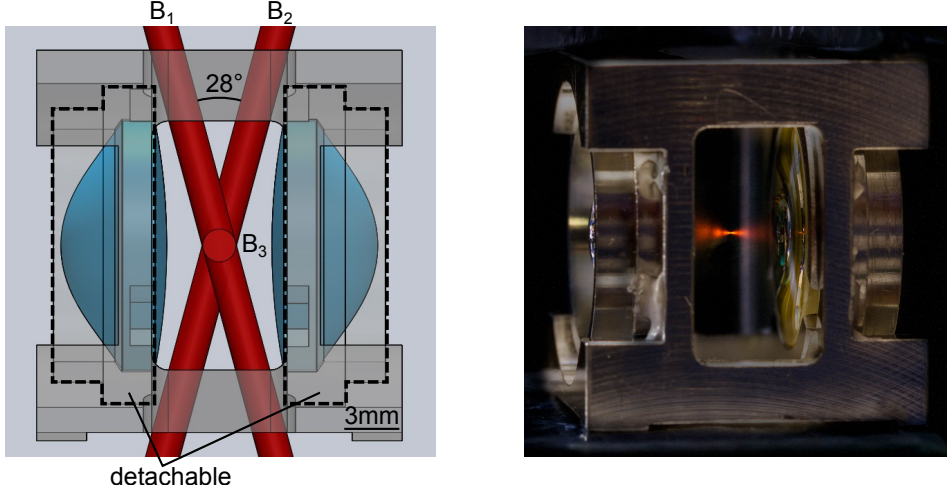


Fig. 2.2 (Left) Schematic of the lens pair mounted on an aluminium holder. Beams $B_{1,2,3}$ consist of 780 nm cooling light and 795 nm repumping light of which B_3 is orthogonal to B_1 and B_2 . (Right) Photograph showing a visible path of 780 nm probe light tightly focused by the lens. (Credit: A. Cere)

in a confocal arrangement with a precision alignment stage. The lens mounts are finally fixed to the main frame with a ultra-high vacuum compatible epoxy (Torr Seal).

2.2.2 Light-atom interaction strength

Now let us further examine the implication of the aforementioned lens properties in the context of light-atom interaction. In a free-space light-atom interface, the interaction strength can be characterised by the coupling efficiency Λ . In our experiment, we drive a circular dipole transition ($5^2S_{1/2}, F = 2, m_F = -2 \rightarrow 5^2P_{3/2}, F' = 3, m_{F'} = -3$) with circularly polarized light. At such, the coupling efficiency Λ can be understood as a geometric quantity describing the spatial mode overlap between the input probe mode and the atomic dipole mode:

$$\Lambda = \frac{|\int \mathbf{E}_p^* \cdot \mathbf{E}_\mu \sin \theta d\theta d\phi|^2}{\int |\mathbf{E}_p|^2 \sin \theta d\theta d\phi \int |\mathbf{E}_\mu|^2 \sin \theta d\theta d\phi}, \quad (2.1)$$

where \mathbf{E}_p is the probe electric field, \mathbf{E}_μ is the dipole electric field distribution and the overlap is integrated over the solid angle covered by the focusing optics. The maximum value of $\Lambda = 1$ represents complete spatial mode overlap.

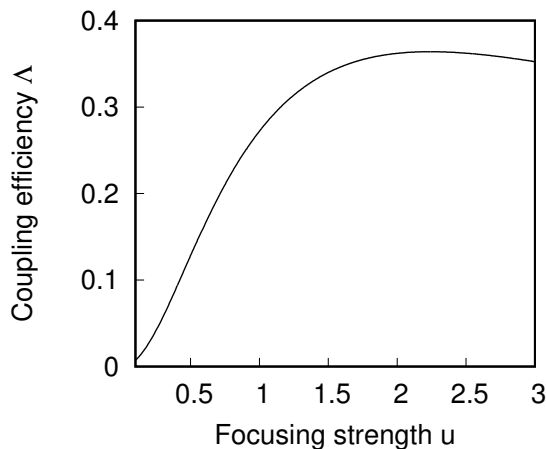


Fig. 2.3 Theoretically expected coupling efficiency for focusing a circularly polarized Gaussian mode with an ideal lens onto a stationary atom following Eq. (2.2).

Following [39, 64], the coupling efficiency Λ of a circularly polarized Gaussian mode focused by an ideal lens to the dipole mode of a stationary atom is given by

$$\Lambda = \frac{3}{16u^3} e^{2/u^2} \left[\Gamma\left(-\frac{1}{4}, \frac{1}{u^2}\right) + u\Gamma\left(\frac{1}{4}, \frac{1}{u^2}\right) \right]^2, \quad (2.2)$$

where $\Gamma(a, b)$ is the incomplete gamma function. The focusing strength u is defined as

$$u := w_{\text{in}}/f, \quad (2.3)$$

where w_{in} is the input beam waist at the lens and f is the focal length. We estimate an upper bound of $\Lambda = 16.7\%$ for our system with focusing strength of $u = 0.61$ when used with 0.1% clipping loss from the lens aperture.

2.2.3 Preliminary test

Operating these lenses at the diffraction limit requires careful optical alignment. Therefore, we first examine the attainable focusing performance of the lenses at the best possible configuration before mounting them in the vacuum chamber. We measure the beam waist at the focus for 780 nm probe light with the knife edge technique [65, 66] and also optimise the alignment on this parameter.

We test three of the custom aspheric lenses (labelled as SL16, SL18, SL19). The spatial mode of the incident probe light is approximately Gaussian given that it is derived from a single-mode fibre. We vary and measure the input beam waist

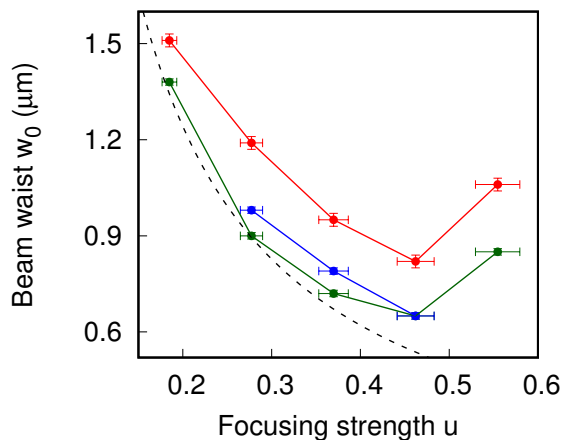


Fig. 2.4 Measured beam waist (bottom) using the knife edge technique for lens SL16 (blue), SL18 (red), SL19 (green) and C230 (grey) with a varying incident beam waist. Dashed line represents the expected beam waist after a lens for a given focusing strength using the paraxial approximation: $w_0 = \lambda / \pi u$, where λ is the wavelength of the beam.

before the test lens by employing different sets of collimation lens and beam expander (Fig. 2.4). Surprisingly, the minimum waist of 650(10) nm is achieved with $u = 0.46$ instead of the largest $u = 0.55$. As a result, we may not use the full aperture and the measured waist of 650 nm suggests an effective focusing strength of $u = 0.38$, and thus $\Lambda = 8.5\%$. We proceed to set up a lens pair with SL16 and SL19, noting the imperfection, which hints at the existence of optical aberration. In the actual experiment, we use a compact triplet fibre collimator (Thorlabs TC25FC-780) which gives a beam waist of 2.7 mm ($u = 0.45$).

2.3 Vacuum system

The trapping lifetime of atoms in optical dipole traps is primarily limited by collisions with the background gas; therefore, an ultra-high vacuum environment is essential to achieve a long trapping time [67–69]. We use a vacuum chamber with a bonded glass cuvette (Hellma OG glass) to house the aspheric lens pair in a compact manner with optical access from all directions. The glass cuvette has a dimension of $3\text{ cm} \times 3\text{ cm} \times 7\text{ cm}$, a wall thickness of 2.5 mm, and is anti-reflection coated on the outer surface for 500 – 1100 nm. Thermal rubidium vapour is provided by a built-in rubidium dispenser (SAES Getters RB/NF/4.8/17 FT10+10) heated electrically with a current

2.4. Laser system

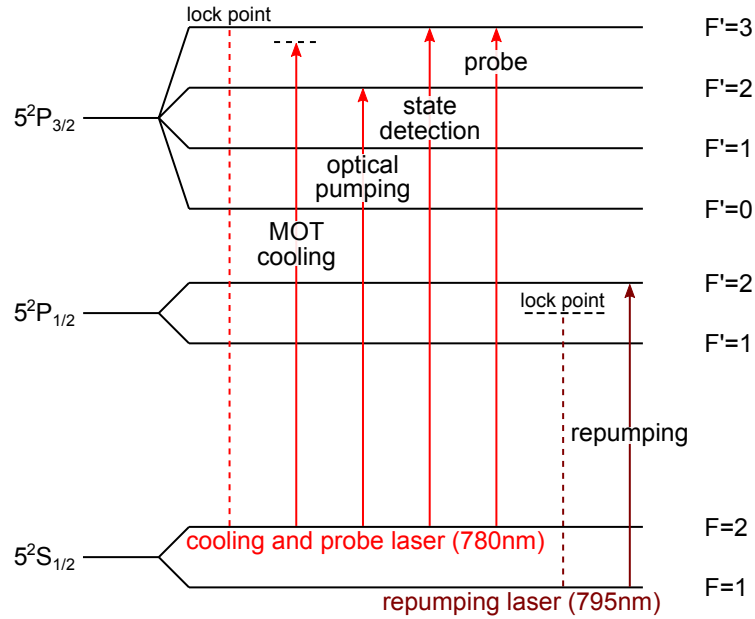


Fig. 2.5 An overview of the laser frequencies used in this experiment. All frequencies are shifted from the laser lock point with acousto-optic modulators. This drawing is not to scale.

at 2 A. The pressure in the vacuum chamber is maintained at 10^{-10} mbar using an ion pump (Agilent Varian Starcell, 20 L/s).

2.4 Laser system

Laser light is used for cooling, trapping, state manipulation, and probing of the atom. Four lasers are used for this experiment to address ^{87}Rb atoms: (1) a cooling and probe laser at 780 nm, (2) a repumping laser at 795 nm, (3) a dipole trap laser at 850 nm, and (4) a secondary dipole trap laser at 760 nm. An illustrative overview to depict the lasers along with the atomic transition of ^{87}Rb is shown in Fig. 2.5.

Specifically, our cooling (probe) and repumping lasers are home-built external cavity diode lasers (ECDL) in a Littrow configuration [70, 71] for which the technical details have been covered in a previous thesis [63]. All laser beams are split into different paths for each purpose, with a dedicated acousto-optic modulator (AOM) for switching and frequency tuning (Fig.2.6). In the following section, we briefly describe the purpose of each laser.

2.4. Laser system

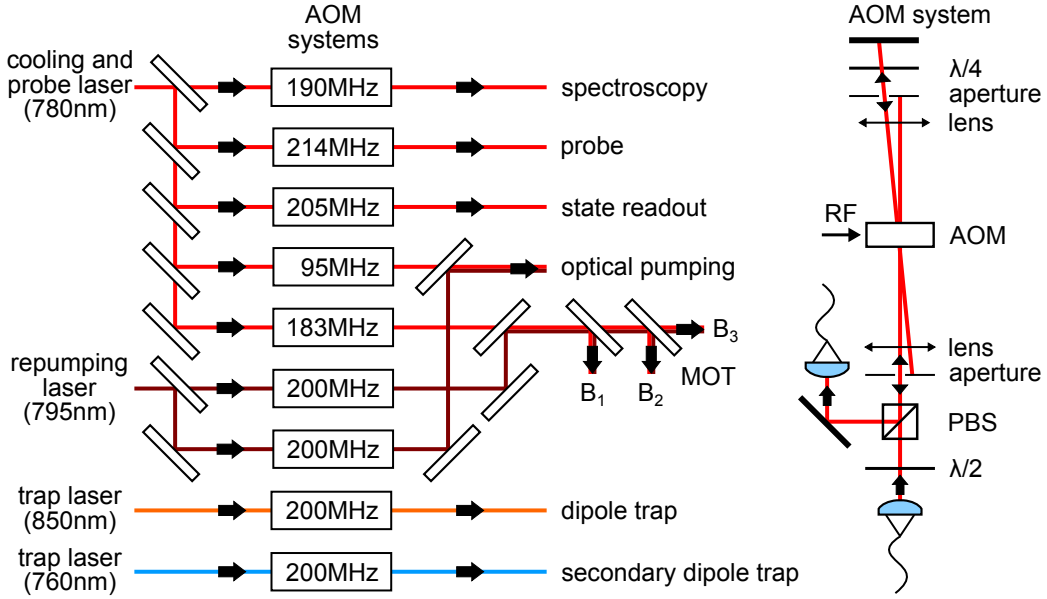


Fig. 2.6 An overview of the frequencies of the acousto-optic modulators (AOMs) used in this experiment. Each AOM is built in a double-pass configuration for switching with an extinction of about 40 dB and frequency tuning (increasing). We use 200 MHz AOMs (Gooch & Housego 3200-124) for everything except a 130 MHz AOM (IntraAction ATM-1331A2) for optical pumping. The exact frequencies for probe, state readout, and optical pumping are tuned depending on the external frequency shifts. MOT: magneto-optical trap, B_{1,2,3}: MOT beams, λ/4: quarter-wave plate, λ/2: half-wave plate, RF: radio frequency, PBS: polarizing beam splitter, lens: f=150 mm.

Cooling and probe laser (780 nm)

We use a 780 nm laser (Sanyo DL-7140-201W) to address the ^{87}Rb D₂ transition ($5^2S_{1/2} \rightarrow 5^2P_{3/2}$) for several purposes: (1) laser cooling and formation of the magneto-optical trap (MOT), (2) optical pumping, (3) excitation for fluorescence detection, and (4) probing light-atom interaction. The laser is frequency-locked to $F = 2 \rightarrow F' = 3$ transition by a modulation transfer spectroscopy (MTS) [72–74]. Prior to locking, the laser frequency is deliberately increased by 390 MHz via an AOM. In this way, the effective laser frequency is 390 MHz below the $F = 2 \rightarrow F' = 3$ transition and can be tuned to resonance using another AOM. The frequency choice is historical to preserve similar AOM settings as the laser was previously locked to $F = 2 \rightarrow F' = 1$ transition by a frequency-modulation (FM) spectroscopy [75, 76]. We find that the MTS spectroscopy performs more stably than a FM spectroscopy, with which our laser stays locked for days.

2.5. Magneto-Optical Trap (MOT)

Repumping laser (795 nm)

As the cooling laser drives the $5^2S_{1/2}, F = 2 \rightarrow 5^2P_{3/2}, F' = 3$ transition, there is a probability of off-resonant excitation to the $5^2P_{3/2}, F' = 2$ level. From there, it can decay into the $5^2S_{1/2}, F = 1$ ground state which takes the atom out of the cooling cycle due to the large hyperfine splitting of 6.8 GHz between the two ground states. Thus, to repopulate the atoms into the $5^2S_{1/2}, F = 2$ state, we employ a 795 nm laser (Thorlabs LD808-SA100) to address the D₁ transition ($5^2S_{1/2} \rightarrow 5^2P_{1/2}$). This repumping process is essential for laser cooling, formation of the MOT, and optical pumping. Our repumping laser is frequency-locked to $F = 1 \rightarrow F' = 2, F' = 1$ crossover signal by a FM spectroscopy.

Dipole trap laser (850 nm)

Our red-detuned far-off-resonant optical dipole trap (FORT) was initially a home-built ECDL (Thorlabs L852P150) running at 852 nm. As the experiment progresses, this laser could not remain single-mode over few hours which significantly affected the stability of light-atom coupling efficiency. We later switched to a distributed feedback laser (Eagleyard EYP-0852-00150) for a more reliable single-mode operation at 851 nm. The change greatly increased the stability and reliability of the experiment. To stabilise the trapping potential, we lock the power of this laser with a control loop feedback into the RF power supplied to the AOM. No frequency stabilisation is required given that the influence on the trapping potential is negligible. The home-built ECDL is only used in the experiment that is described in Chapter 4.

Secondary dipole trap laser (760 nm)

For the experiment described in Chapter 5, we required a stronger confinement of the atom in the axial direction. To increase the axial trapping frequency, we used an additional blue-detuned FORT in standing wave configuration. The rationale for a blue-detuned FORT is to avoid an additional light shift induced by the trap (see Section 3.1.1 for details on light shift). Our blue-detuned FORT is also formed by a distributed feedback laser (Eagleyard EYP-0760-00040), which operates at 760 nm.

2.5 Magneto-Optical Trap (MOT)

A magneto-optical trap (MOT) cools and traps atoms simultaneously and thereby forms a cold and dense cloud of atoms. The MOT is formed by three pairs of

2.5. Magneto-Optical Trap (MOT)

counter-propagating laser beams and a magnetic quadrupole field with a minimum at the intersection point. This section briefly describes the implementation of our MOT. A comprehensive description of the underlying working principle can be found in Ref. [77, 78].

2.5.1 MOT beams

The MOT beams consist of 780 nm cooling light and 795 nm repumping light (Fig. 2.5): The cooling light is red-detuned $\sim 2.3\Gamma_0$ with respect to the $5^2S_{1/2}, F = 2 \rightarrow 5^2P_{3/2}, F' = 3$ closed transition, where $\Gamma_0 = 2\pi \cdot 6.065(9)$ MHz is the natural linewidth [79]. The repumping light, utilised to depopulate the $5^2S_{1/2}, F = 1$ state, is nearly resonant to the $5^2S_{1/2} \rightarrow 5^2P_{1/2}$ transition. The MOT beams are circularly polarized and retroreflected to form three pairs of counter-propagating beams with opposite polarization. The geometrical orientation of these beams are shown in Fig. 2.2. Two of these vertical beams, B_1 and B_2 , intersect at an angle of 28° , and thus have a propagation component along the direction of the trapping beam to ensure cooling along that axis. They carry cooling light at an intensity of ~ 16 mW/cm² and repumping light of ~ 30 mW/cm² with a beam waist of 1 mm. The horizontal beam B_3 is orthogonal to these two beams and carries twice as much power. We use the same light not only for the MOT but also for subsequent polarization gradient cooling (PGC, see Chapter 3).

2.5.2 Magnetic quadrupole field

The magnetic quadrupole field needed for a MOT is generated by a pair of coils arranged in anti-Helmholtz configuration. Built with an inner diameter of 5.5 cm, an outer diameter of 7.5 cm, and 200 turns of insulated copper wire, the coils are expected to produce a gradient of approximately 4 mT/cm at an operating current of 2A. In addition, we use three pairs of Helmholtz coils, one for each orthogonal axis, to compensate for external magnetic field, to a residual value about $4 \mu\text{T}$. Figure 2.7 shows a photograph of the experimental setup. To view the atom clouds formed by the MOT, we use a Point Grey CCD camera (CMLN-13S2M-CS, 1296×964 pixel, $3.75 \mu\text{m}$ pixel size) and a times two magnification imaging telescope.

2.6. Far-off-resonant optical dipole trap

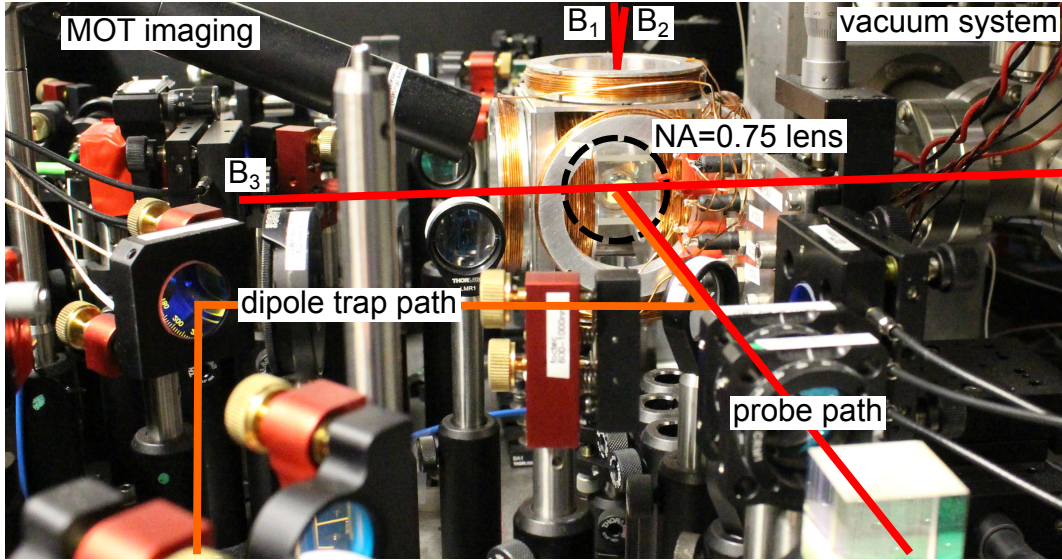


Fig. 2.7 Photograph of our experimental setup to probe light-atom interaction. $B_{1,2,3}$: MOT beams.

2.6 Far-off-resonant optical dipole trap

A far-off-resonant optical dipole trap (FORT) for atoms operates based on the interaction of the atomic dipole moment with the intensity gradient of a far-off-resonant light field [80, 81]. The interaction of the light with the atom induces AC Stark shifts in the atomic energy levels proportional to the light intensity. For red-detuned light with respect to the atomic transition, the interaction is attractive. Therefore, focusing red-detuned light creates a potential well that attracts the atom into it. Far-off-resonant light is employed to minimise the scattering by the atom because the depth of the potential scales as I/δ , whereas the scattering rate is proportional to I/δ^2 . Here, I refers to the intensity of the trapping light, and δ is the detuning from the atomic transition. A more detailed description can be found in Ref. [81].

By setting up the FORT in a tightly focused configuration, it can be used to exclusively trap a single neutral atom [82]. The number of atoms is ensured to be either zero or one via the collisional blockade mechanism: whenever two or more atoms are trapped in the presence of cooling light, they undergo light-induced collisions resulting in either zero or one atom in the trap [83].

2.6. Far-off-resonant optical dipole trap

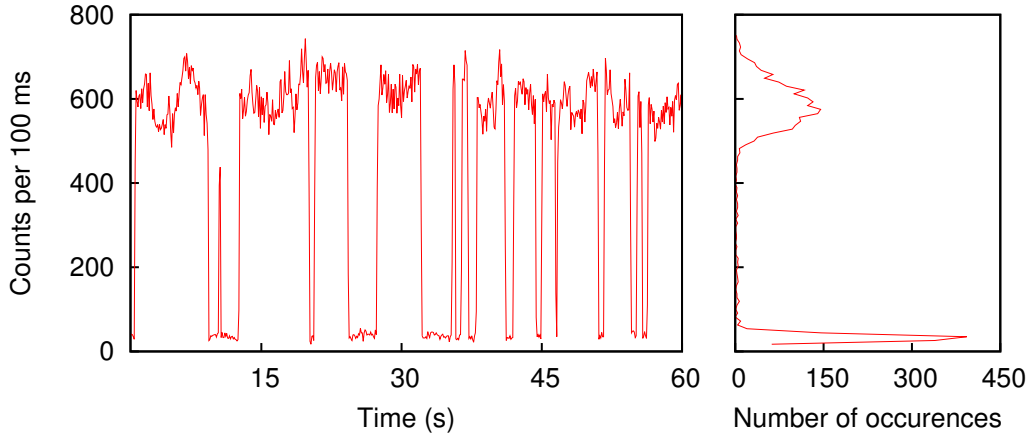


Fig. 2.8 Fluorescence of single atoms in an optical dipole trap under continuous illumination of the MOT beams. (Left) Typical telegraph signature of single atom fluorescence over time. (Right) Histogram of the single atom fluorescence for the time trace (left) extended to five minutes.

2.6.1 Implementation

Our FORT is formed by tightly focusing light at 851 nm using the same aspheric lens for probing light-atom interaction. Originating from a single mode fibre, the beam is focused down to a waist of approximately $1.4 \mu\text{m}$. We typically operate the trap at a depth of $U_0 \simeq k_B \times 2 \text{ mK}$ with a laser power of about 15 mW. For loading and laser cooling of atoms, the trap is linearly polarized; for probing light-atom interaction, the trap is circularly polarized (see Chapter 3).

Exploiting the collisional blockade mechanism, we load a single ^{87}Rb atom into the FORT directly from the MOT by overlapping the two traps. The fluorescence from the atom is collected by the aspheric lens pair into single mode fibres and then detected using avalanche photodetectors (APDs, Perkin Elmer SPCM-AQR-15). These APDs have detection efficiencies of 59(3)% and 56(4)% at 780 nm and dark count rates of 300 cps and 155 cps, respectively. Figure 2.8 shows the typical signature of sub-Poissonian loading of single atoms with either zero or one atom trapped. To prolong the trapping lifetime of the atoms, we avoid further loading events by switching off the magnetic quadrupole field to disperse the MOT cloud. The atom loading sequence is implemented with a trigger using the telegraph-like fluorescence signal of a single atom.

2.6. Far-off-resonant optical dipole trap

2.6.2 Characterisation

For a Gaussian potential, the trap frequencies in the radial and axial directions are, respectively,

$$\omega_r = \sqrt{\frac{4U_0}{mw_0^2}}, \quad \omega_z = \sqrt{\frac{2U_0}{mz_R^2}}, \quad (2.4)$$

where U_0 is the trap depth, m the mass of ^{87}Rb , w_0 the beam waist, and z_R the Rayleigh range [81]. In principle, w_0 is given directly by the trapping beam profile and the focusing optics. However, that requires the optics to be aberration free, which is unlikely in our case because the aspheric lens was designed for 780 nm. Consequently, we measure U_0 and the trap frequencies independently, which allows us to infer w_0 at the trap.

The trap depth U_0 can be obtained from the AC Stark shift induced by the trap on the atom. Probing the $5^2S_{1/2}, F = 2, m_F = -2 \rightarrow 5^2P_{3/2}, F' = 3, m_{F'} = -3$ transition, we measure a shift of 48.03(3) MHz from the natural transition frequency (Fig. 4.3). Taking into account also the Zeeman shift, and comparing to the AC Stark shift calculation [84, 85], we deduce a trap depth $U_0 = k_B \times 2.22(1)$ mK.

To measure the trap frequencies, we parametrically heat the atoms by modulating the trap laser power through our AOM (Fig. 2.9). Scanning the modulation frequency $\omega_m/2\pi$, we observe a reduction in atom survival probability in the trap at the parametric resonance frequency [86]

$$\omega_n = \frac{2\omega_{r/z}}{n}, \quad (n = 1, 2, 3, \dots). \quad (2.5)$$

This signal, however, is incapable of resolving the axial trap frequency in our case. As the light-atom interaction also depends on the temperature of the atom, we use instead the transmission of a resonant probe light (see Section 4.1) as a signal. From the parametric resonance, we deduce radial frequencies $\omega_r/2\pi = 107(1)$ kHz, $\omega_{r'}/2\pi = 124(1)$ kHz and an axial frequency $\omega_z/2\pi = 13.8(1)$ kHz. The existence of two distinct radial frequencies suggests an elliptical beam waist at the focus. Nevertheless, ω_r and ω_z satisfy the relation from a Gaussian beam profile which gives a beam waist of $1.4 \mu\text{m}$ for our measured trap depth.

2.6.3 Trapping lifetime

We determine the lifetime of single atoms in our dipole trap from their survival probability after a certain duration. This measurement is repeated under several

2.6. Far-off-resonant optical dipole trap

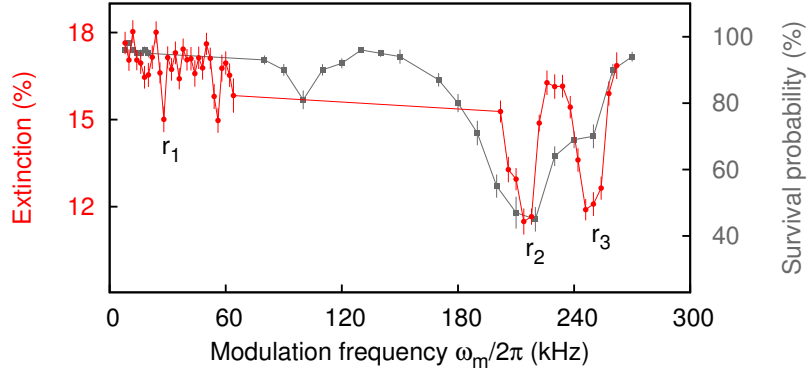


Fig. 2.9 Trap frequency measurement via parametric heating of atoms. Occurrence of parametric resonance at two times the trap frequency reduces the resonant extinction (red) and survival probability (grey) of atoms in the FORT. Parametric resonance: $r_1=2\omega_z/2\pi$, $r_2=2\omega_r/2\pi$, and $r_3=2\omega_{r'}/2\pi$, where $\omega_z/2\pi = 13.8(1)$ kHz, $\omega_r/2\pi = 107(1)$ kHz, and $\omega_{r'}/2\pi = 124(1)$ kHz.

conditions: linearly polarized trap, circularly polarized trap, with and without continuous illumination of the MOT beams. The result is shown in Fig. 2.10. The best trapping lifetime of 9.3(5) s is obtained in the linearly polarized trap without continuous illumination of the MOT beams, and is reduced to 4.5(2) s when the MOT beams are on. In the circularly polarized trap, the lifetime is significantly lower and the atom has a reduced maximum survival probability of 80%. Especially under continuous illumination of the MOT beams, the lifetime is merely 0.55(3) s. When the MOT beams are off, there are two characteristic decay times: a fast decay at 0.54(7) s and a slow decay at 11(1) s. The fast decay time, which is the same as the trapping lifetime under continuous illumination, results from probing the atom's presence with a short illumination.

The stark difference of trapping lifetimes in the two different trap polarization under continuous illumination prompts for further investigation. A closer look reveals that our non-orthogonal MOT beams have different amount of σ^+ and σ^- light in the forward and backward direction along the quantization axis (Fig. 2.11). This, together with the asymmetrical shift in the $5^2P_{3/2}$ hyperfine states caused by a circularly polarized dipole trap (Fig. 3.1) induces a difference in radiation pressure on the atom. To reduce this deleterious effect, we redistribute some of the power from the vertical MOT beams into the horizontal beam. Figure 2.12 shows the improvement of trapping lifetime under continuous illumination doubling to 1.14(5) s, with an increased maximum survival probability to 96%. Note that these

2.6. Far-off-resonant optical dipole trap

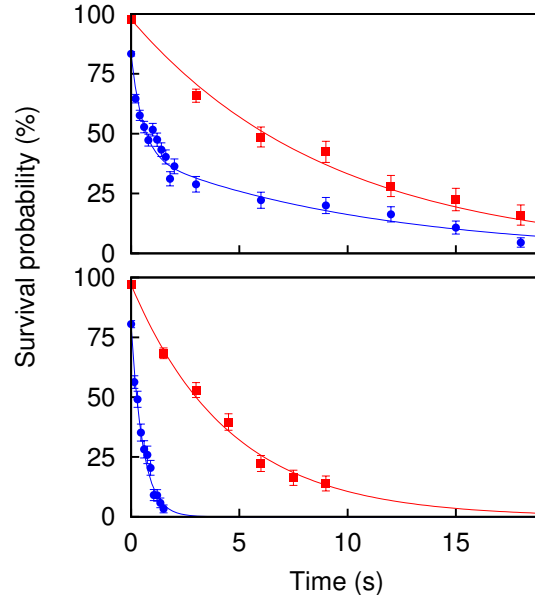


Fig. 2.10 Trapping lifetime of single atoms in a linearly (red square) and a circularly (blue circle) polarized dipole trap. (Top) Without continuous illumination of MOT. (Bottom) Same as top but under continuous illumination of MOT. Solid lines are exponential fits. Error bars represent standard error of binomial statistics accumulated from 100-2000 repeated sequences.

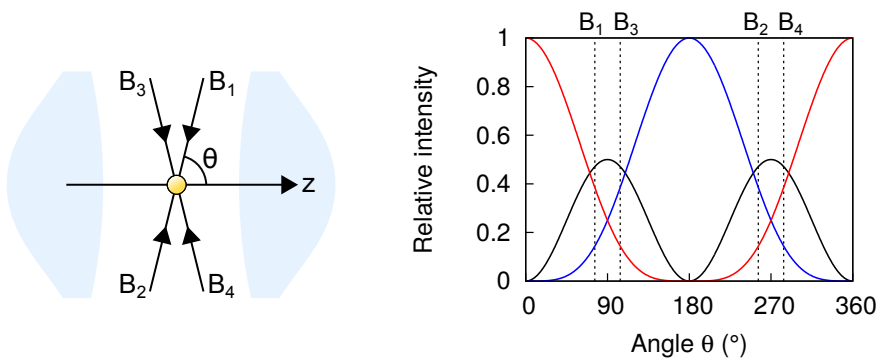


Fig. 2.11 (Left) Beam layout for the vertical MOT beams. θ depicts the angle between a beam and the quantization axis z defined by the FORT. (Right) Polarization decomposition of circularly polarized MOT beams (along its propagation direction) onto the quantization axis z as circular σ^+ (red), σ^- (blue) and linear π (black).

2.7. Manipulation of single atoms

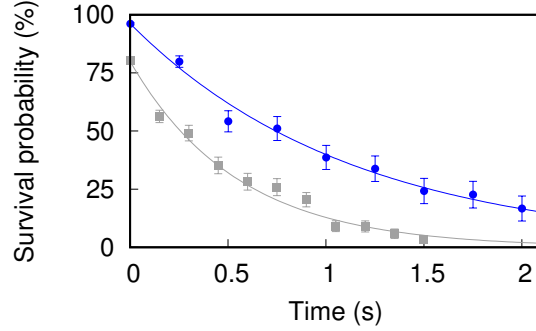


Fig. 2.12 Lifetime of single atoms in a circularly polarized trap under continuous illumination before (grey square) and after (blue circle) redistribution of MOT beams power. Prior to redistribution, the vertical MOT beams are $300 \mu\text{W}$ and horizontal beams are $250 \mu\text{W}$; after redistribution, the beams are $150 \mu\text{W}$ and $600 \mu\text{W}$, respectively. Solid lines are fits to exponential function. Error bars represent standard error of binomial statistics accumulated from 100-2000 repeated sequences.

characterisation measurements were performed in an early stage of this experiment. We later operate the dipole trap for loading atoms in linear polarization for a more efficient laser cooling scheme (see Chapter 3). The trap polarization is switched in situ to circular polarization only during the light-atom coupling experiment.

2.7 Manipulation of single atoms

2.7.1 State-selective detection

We adopt a loseless state-selective detection scheme described in [87, 88] as part of our toolbox to determine the hyperfine state of the atom. In accordance to the scheme, we detect the atomic fluorescence while driving the $5^2S_{1/2}, F = 2 \rightarrow 5^2P_{3/2}, F' = 3$ transition. Atoms in the $5^2S_{1/2}, F = 2$ (bright) state scatter light, as opposed to atoms in the $5^2S_{1/2}, F = 1$ (dark) state, and therefore reveal their hyperfine state through the brightness of the fluorescence.

To determine the state detection efficiency of the atom, we measure the photon distribution of the atom for both bright and dark state (Fig. 2.13). A convenient quantity to characterise the detection performance is the state readout fidelity

$$F = 1 - \frac{1}{2}(\epsilon_b + \epsilon_d), \quad (2.6)$$

2.7. Manipulation of single atoms

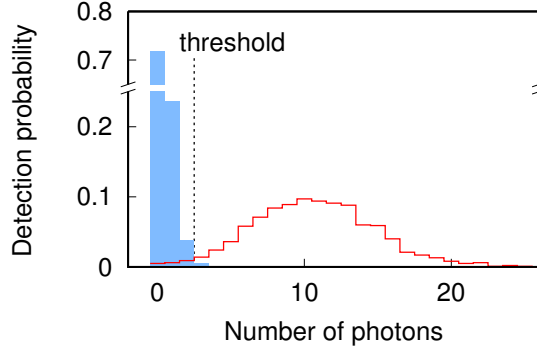


Fig. 2.13 Histogram for photon detection probability for atoms prepared in a bright state (red) and a dark state (blue), respectively. The state readout fidelity is 98.6(1)% for a set threshold of 3 detected photons.

where ε_b is the fraction of experiments in which an atom prepared in the bright state is identified to be dark, and conversely for ε_d [89]. To minimise off-resonant scattering events caused by the optical dipole trap, we reduce the operating depth to about $U_0 = k_B \times 1.6$ mK. The probe light is near resonant with an intensity of about 0.6 W/m². To determine the readout fidelity at different scattered photon numbers, we vary the probe duration from 0.3 to 2.7 ms (Fig. 2.14). As the pulse length increases, the mean detected photons in the bright state $\langle n_b \rangle$ increases at the expense of the atom survival probability. However, the readout fidelity nearly saturates already at $\langle n_b \rangle = 11$ with 98.6(1)%, and peaks at $\langle n_b \rangle = 19$ with 99.0(2)%. This is consistent with the bright state distribution becoming increasingly non-Poissonian as characterised by the Fano factor¹, which is related to shot-to-shot differences in photon collection rate.

2.7.2 Optical pumping

Throughout this thesis, we probe the light-atom interaction by driving the closed transition $5^2S_{1/2}, F = 2, m_F = -2 \rightarrow 5^2P_{3/2}, F' = 3, m_F = -3$. To ensure that the atom is initialised in the $5^2S_{1/2}, F = 2, m_F = -2$ state, we perform optical pumping by simultaneously sending two circularly σ^- polarized light beams on resonance with the $5^2S_{1/2}, F = 2, \rightarrow 5^2P_{1/2}, F' = 2$ and the $5^2S_{1/2}, F = 1, \rightarrow 5^2P_{3/2}, F' = 2$ transitions, respectively (see Fig. 2.15). Driving these transitions successively, the atom is in the desired $5^2S_{1/2}, F = 2$ state, which is decoupled from the pumping

¹The Fano factor is defined as $(\Delta n)^2 / \langle n \rangle$, where Δn is the standard deviation and $\langle n \rangle$ is the mean of the distribution. For a Poissonian distribution, the Fano factor is exactly 1.

2.7. Manipulation of single atoms

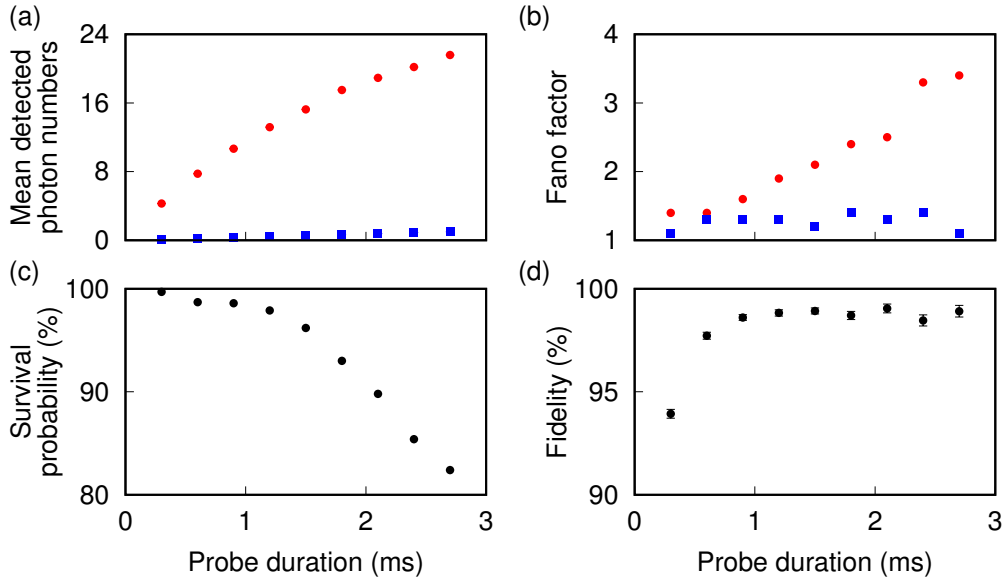


Fig. 2.14 (a) Mean detected photon numbers and (b) Fano factor computed from the photon distribution of the atom prepared in bright state (red circles) and dark state (blue squares), respectively. (c) Atom survival probability after detection and (d) state readout fidelity over probe duration.

light. Such a pumping scheme prepares the atom in the desired state with a minimal number of excitations, and thus avoids unnecessary heating. We typically perform optical pumping for 5 ms. Detailed experimental sequences will be presented along with each individual experiments later in the following chapters.

2.7. Manipulation of single atoms

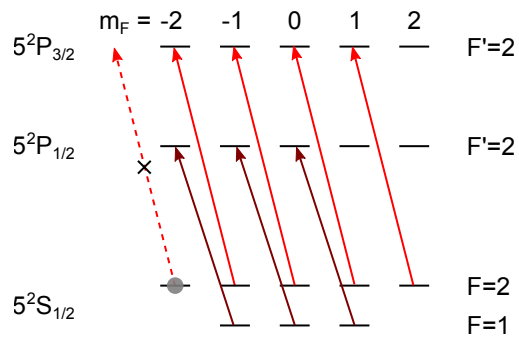


Fig. 2.15 Optical pumping scheme to prepare atoms in the $5^2S_{1/2}, F = 2, m_F = -2$ state. The atoms, upon reaching the $5^2S_{1/2}, F = 2, m_F = -2$ state, are decoupled from the pumping light as no allowed transition exists. The light-red (dark-red) arrows indicate circularly σ^- polarized 780 nm (795 nm) light tuned near resonance to the driven transition.

Chapter 3

Polarization gradient cooling in optical dipole traps

This chapter presents the investigation of polarization gradient cooling (PGC) of a single ^{87}Rb atom in a tightly focused far off-resonant optical dipole trap (FORT). First, we briefly introduce PGC and qualitatively explain how it is affected by the light shifts induced by the trapping field. Next, we describe the experimental realisation and the details of the atom temperature measurements. We then present the results and show that the cooling limit strongly depends on the polarization of the trapping field. Finally, we demonstrate that switching the trap polarization from linear to circular after PGC induces only minor heating. A majority of the content in this chapter has been published in [58]¹.

3.1 Introduction

Optically confined atoms, like free atoms, can be cooled to sub-Doppler temperatures by polarization gradient cooling (PGC) [90–92]. Efficient PGC enables further cooling to the vibrational ground state by Raman sideband cooling [93–95]. However, despite its practical relevance, the influence of the optical trap on the efficiency of PGC is relatively unexplored; for example, reported temperatures for the commonly used atomic species ^{87}Rb vary by an order of magnitude for similar experimental configurations [96, 97, 93].

¹Y.-S.C. and M.S. conceived and performed the experiments, as well as analysed the data. C.K. supervised the project. All authors discussed the results and contributed to the writing of the paper.

Here, we consider the configuration of counter-propagating beams of opposite circular polarizations, referred to as $\sigma^+ - \sigma^-$ PGC². Shortly after the initial demonstrations of $\sigma^+ - \sigma^-$ PGC, it became clear that, while this cooling technique is in general robust against small variations of the experimental parameters, it is very sensitive to magnetic fields [98–103]. The reason for the detrimental effect of magnetic fields is that $\sigma^+ - \sigma^-$ PGC is based on velocity-selective Raman transitions, which redistribute population within the spin states of the ground state manifold. The associated Zeeman effect shifts the Raman resonance, and thus the atoms are no longer cooled toward zero velocity but to a finite velocity at which the Doppler shift compensates the Zeeman shift.

3.1.1 Effect of light shifts on PGC

The energy levels of the cooling transition are shifted for an atom in a FORT. In our experiment $\sigma^+ - \sigma^-$ PGC of ^{87}Rb atoms is performed on the closed $5^2S_{1/2}, F = 2 \rightarrow 5^2P_{3/2}, F' = 3$ transition near 780 nm. In the following, we consider the energy shifts caused by a red-detuned FORT at 851 nm with detuning $\delta_1 = 2\pi \times 2.48 \times 10^{13} \text{ rads}^{-1}$ and $\delta_2 = 2\pi \times 3.21 \times 10^{13} \text{ rads}^{-1}$ from the ^{87}Rb D_1 and D_2 lines, respectively. The light shift of the ground state manifold $5^2S_{1/2}, F = 2$ can be written in a compact form [104, 105, 94]

$$U = -U_0 \left(1 + \frac{\delta_2 - \delta_1}{\delta_2 + 2\delta_1} \mathbf{C} \cdot g_F \mathbf{F} \right), \quad (3.1)$$

where U_0 is the scalar light shift or ‘trap depth’, \mathbf{F} the total angular momentum operator, and $g_F = [F(F+1) - I(I+1) + J(J+1)]/F(F+1)$ the Landé-factor. The vector $\mathbf{C} = \text{Im}(\boldsymbol{\epsilon} \times \boldsymbol{\epsilon}^*)$, where $\boldsymbol{\epsilon}$ is the (unit norm) polarization vector, quantifies the ellipticity of the dipole field. In a linearly π -polarized trap ($|\mathbf{C}| = 0$), all spin states within the ground state manifold are shifted equally as the tensorial shift is negligible for far off-resonant trapping fields [104–106]. This degeneracy is lifted in an elliptically polarized trap. For a circularly σ^+ -polarized trap ($|\mathbf{C}| = 1$), the trapping field acts as a ‘fictitious magnetic field’ pointing in the direction of propagation [107]. From Eq. (3.1), we find that a σ^+ -polarized trap of depth $U_0 = k_B \times 1 \text{ mK}$ produces a shift of 890 kHz between adjacent spin states, equivalent to the shift caused by a magnetic field of strength 0.13 mT.

²For detailed explanations of the underlying working principle of $\sigma^+ - \sigma^-$ PGC refer to [92].

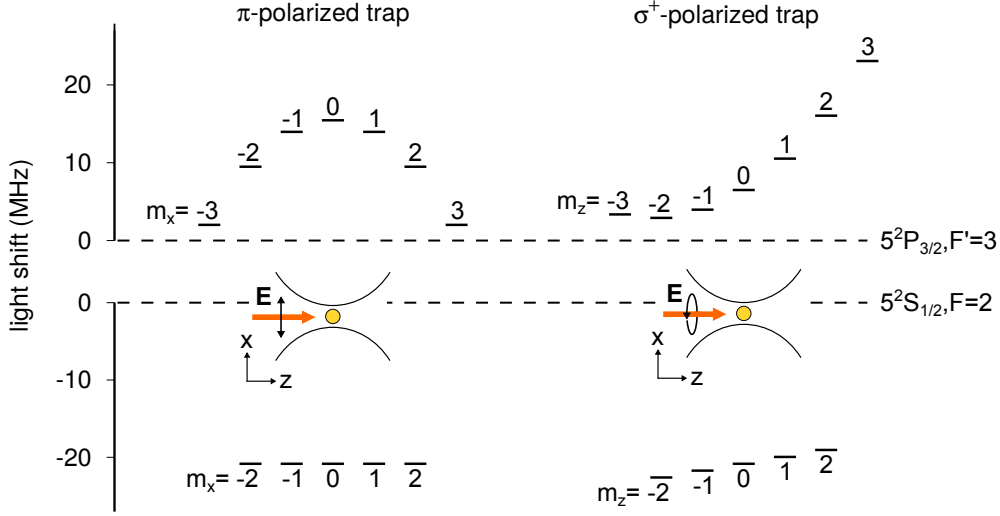


Fig. 3.1 Energy level scheme for the $5^2S_{1/2}, F = 2 \rightarrow 5^2P_{3/2}, F' = 3$ transition near 780 nm of a ^{87}Rb atom in a π -polarized (parallel to x axis) and a σ^+ -polarized FORT. The light shifts are calculated for a FORT operating at 851 nm with a trap depth of $U_0 = k_B \times 1 \text{ mK}$. The quantization axis is defined by the trap polarization: x axis for the π -polarized trap and z axis for the σ^+ -polarized trap, respectively. Inset illustrates the geometrical arrangement: The trapping beam propagates along the z axis with \mathbf{E} denoting the electric field vector.

Both π and σ^+ -polarized light lift the degeneracy of the excited state $5^2P_{3/2}, F' = 3$ manifold. The spin-state dependent energy shifts can be on the order of the trap depth, and therefore can exceed several times the natural linewidth $\Gamma_0 = 2\pi \cdot 6.07 \text{ MHz}$. To accurately calculate the energy shifts for individual states within the hyperfine manifold, one has to consider the contributions from all dipole-allowed transitions [85]. Here we account for the seven most relevant transitions for which the details of the calculations have been outlined in the appendix of [61]. Figure 3.1 shows the calculated light shifts for a π and a σ^+ -polarized FORT operating at 851 nm with a trap depth of $U_0 = k_B \times 1 \text{ mK}$ [84, 85]. Notably, for a π -polarized trap the spins states in the excited state are symmetrically shifted, which is in stark contrast to the highly asymmetric shifts for a σ^+ -polarized trap.

3.1.2 One-dimensional PGC semi-classical simulation

To qualitatively understand the effect of the light shifts on PGC, we calculate the force an atom of fixed velocity experiences when travelling across a $\sigma^+ \text{-} \sigma^-$ PGC field in the FORT. We use a semi-classical description, which defines the force F

3.1. Introduction

on an atom as the expectation value of the quantum mechanical force operator, $F = -\langle \nabla \hat{H} \rangle$ [77]. The total Hamiltonian

$$\hat{H} = \hat{H}_0 + \hat{H}_{\text{int}} \quad (3.2)$$

consists of two parts: (1) a spatially independent Hamiltonian \hat{H}_0 which contains the energy levels of the cooling transition including the light shifts induced by the trap and (2) a Hamiltonian which describes the interaction with the near-resonant PGC field,

$$\hat{H}_{\text{int}} = -\frac{\hbar}{2} (\Omega_+(\vec{r})\hat{A}_+ + \Omega_-(\vec{r})\hat{A}_- + \Omega_\pi(\vec{r})\hat{A}_\pi) + h.c., \quad (3.3)$$

where Ω_+ , Ω_- and Ω_π are the spatially dependent Rabi frequencies for σ^+ , σ^- and π -polarized light, with \hat{A}_+ , \hat{A}_- and \hat{A}_π as the atomic lowering operators for the respective polarizations. For a given atomic velocity, we solve the corresponding master equation,

$$\dot{\rho} = -\frac{i}{\hbar} [\rho, \hat{H}] + \mathcal{L}[\rho] \quad (3.4)$$

by the matrix continued fraction method ($\mathcal{L}[\rho]$ is the Lindblad superoperator accounting for spontaneous emission) [108, 109]. We then compute the steady-state force averaged over the travel through one cycle of the light. The computation is evaluated using the Quantum Optics Toolbox for MATLAB [110, 111].

For a free atom, the simulation shows a steep slope of the force around zero velocity, which is a hallmark of sub-Doppler cooling (Fig. 3.2, black line). For an atom confined in a FORT, the force depends strongly on the trap polarization and the angle between the trapping beam and the PGC field. Figure 3.2 shows the force for two polarizations, linear π along the x axis and circular σ^+ , as well as two directions for the PGC beams, parallel and perpendicular to the trapping beam. In the π -polarized trap [Fig. 3.2(a) and (c)], the persisting steep slope of the force around zero velocity indicates that the PGC is little affected by the trap, aside from a narrowing of the sub-Doppler feature due to the increased detuning from the cooling transition. The σ^+ -polarized trap exhibits five resonances when the propagation direction of the PGC field is perpendicular to the trapping beam [Fig. 3.2(b)]. These velocity selective resonances correspond to Raman transitions between ground state sublevels for $\Delta m_F = 0, \pm 1, \pm 2$ transitions, known from PGC in strong transverse magnetic fields [77, 103]. For a PGC field propagating in parallel to the trapping beam, only one Raman transition can be brought into resonance by the motion of the atom [Fig. 3.2(d)] — a situation which resembles PGC in longitudinal magnetic

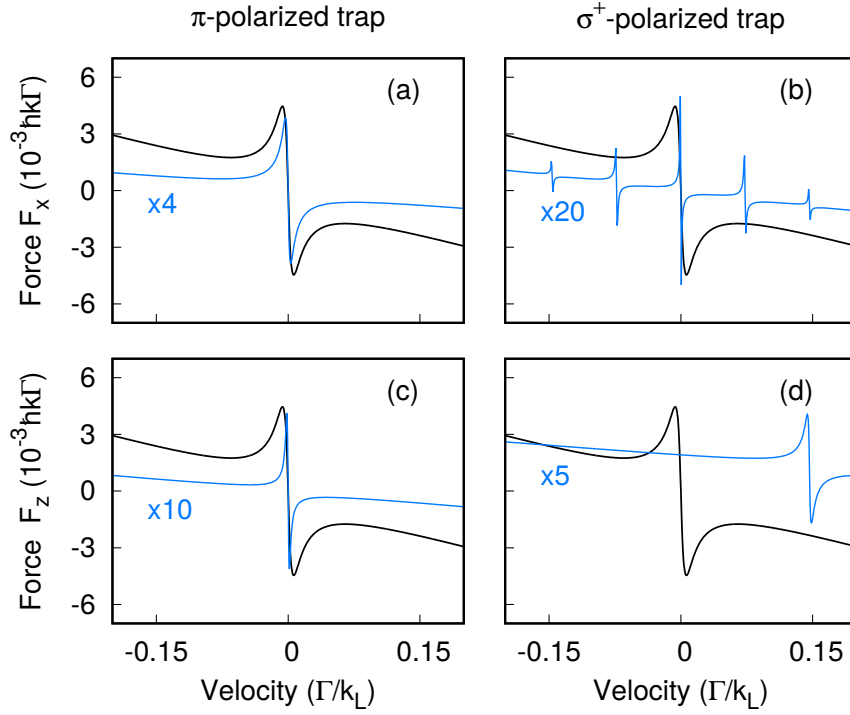


Fig. 3.2 Calculated force on an atom of fixed velocity moving through a $\sigma^+ - \sigma^-$ PGC field for different axes and FORT polarizations. Both beams of the PGC field have a Rabi frequency $\Omega = \Gamma_0/2$ and are red-detuned from the natural transition frequency by $\Delta = -3\Gamma_0$, where $\Gamma_0 = 2\pi \times 6.07$ MHz is the natural linewidth. Black and blue lines indicate the force for a free and a trapped atom, respectively. (a) π -polarized trap, PGC field propagating along x axis. (b) σ^+ -polarized trap, PGC field propagating along x axis. (c) π -polarized trap, PGC field propagating along z axis. (d) σ^+ -polarized trap, PGC field propagating along z axis.

3.2. Experimental realisation

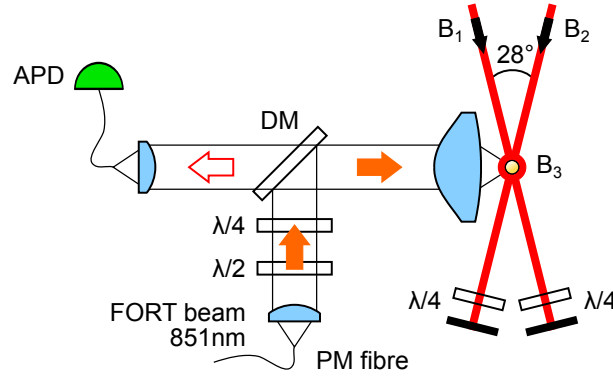


Fig. 3.3 Optical setup for trapping, polarization gradient cooling, and fluorescence detection of a single atom. APD: avalanche photodetector, DM: dichroic mirror, $\lambda/4$: quarter-wave plate, $\lambda/2$: half-wave plate, B: beam consisting of 780 nm cooling light and 795 nm repumping light with a waist of 1 mm. B₃ is perpendicular to B₁ and B₂.

fields [99, 100]. Although this simple 1-D model of the force cannot predict the final temperatures in the actual experiment, it indicates that PGC works in a π -polarized trap, but is strongly compromised in a mK-deep σ^+ -polarized trap.

3.2 Experimental realisation

3.2.1 Optical setup

The experimental setup is the same as presented in Chapter 2. For clarity, we highlight in Fig. 3.3 a simplified version with optical components that are essential for this part and briefly describe the relevant details.

We use the same light for the MOT and PGC, provided by three circularly polarized beams, which are retroreflected with opposite polarization. Two of these beams B₁, B₂ are non-orthogonal, and have a propagation component along the direction of the trapping beam to ensure cooling along that axis. The third beam B₃ is orthogonal to these two beams and carries twice as much power. We reduce the power of these beams during the PGC phase for optimal cooling upon loading a single atom which marks the end of the MOT phase. Moreover, we modulate the mirror position of the cooling beams with an amplitude of 1 μm at 100 Hz to average the interference pattern of the cooling light over the atom position (Fig. 3.4) [93]. The frequency of the cooling light is red-detuned from the natural transition frequency by typically $\Delta = -3\Gamma_0$. In addition, all beams carry repumping light nearly resonant

3.2. Experimental realisation

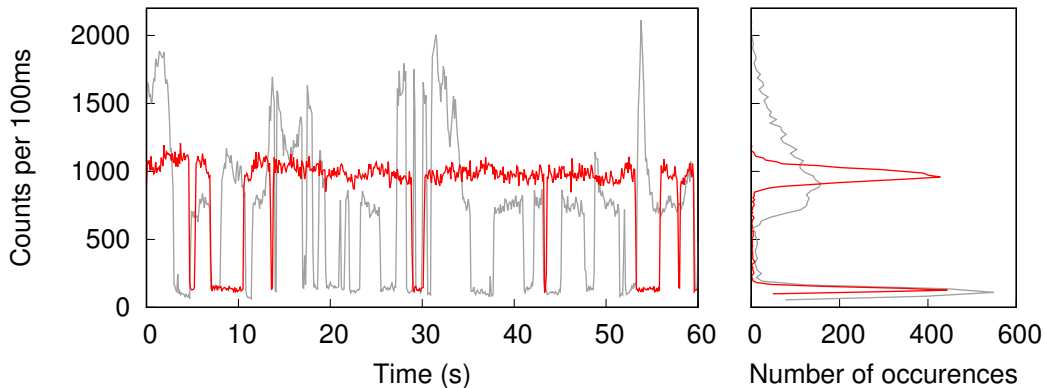


Fig. 3.4 (Left) Fluorescence of single atoms under continuous illumination of cooling beams before (grey) and after (red) implementation of mirror position modulation. Unlike the typical telegraph signature of single atom fluorescence, the largest and lowest rates may differ by more than a factor of two due to slow drifts in the interference pattern of the polarization gradient, which leads to shot-to-shot fluctuation in the final PGC temperature. (Right) Histograms of the single atom fluorescence for time traces (left) extended to eight minutes.

with the D_1 line at 795 nm to clear out the $5^2S_{1/2}, F = 1$ population. Residual magnetic fields are compensated to approximately $4 \mu\text{T}$ at the position of the atom.

Our FORT is formed by 851 nm light and has a depth of $U_0 = k_B \times 1.88(1)$ mK, with radial frequencies $\omega_r/2\pi = 113(1)$ kHz, $\omega_r'/2\pi = 98(1)$ kHz, and an axial frequency $\omega_z/2\pi = 12.6(1)$ kHz. We remark that the large $1.4 \mu\text{m}$ beam waist of our trapping beam ensures that the variation of the polarization near the focal spot is insignificant [112, 93, 94].

3.2.2 Temperature measurement

We measure the temperature of single atoms following the release and recapture method described in [97]: First, the trap is switched off to release the atom. After a variable time, the trap is switched on to recapture the atom. As hotter atoms travel faster, they have a higher probability to escape the trap than colder ones, resulting in a lower recapture probability. By comparing the recapture probabilities to a Monte Carlo simulation of the atom trajectories, the temperature of single atoms over repeated realisations of the same experiment is extracted.

Our experimental sequence is displayed in Fig. 3.5. The experiment is triggered to begin upon the loading of a single ^{87}Rb atom from the magneto-optical trap (MOT) into the dipole trap and then repeats in the following way:

3.2. Experimental realisation

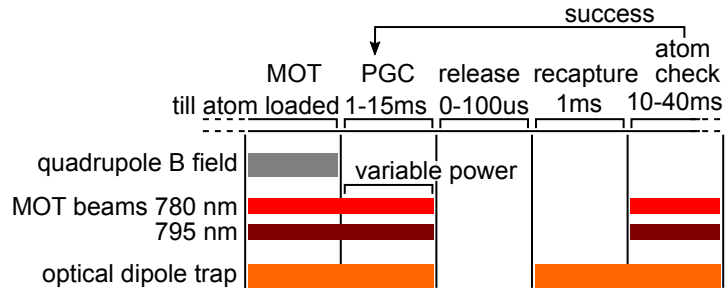


Fig. 3.5 Experimental sequence to perform a release and recapture measurement to probe the temperature of the atom after PGC. We typically release the atom for a set of 11 different intervals. Each sequence is repeated for several hundred times to extract an estimate of the recapture probability.

1. Switch off the quadrupole magnetic field.
2. Perform polarization gradient cooling (PGC) for 1-15 ms with MOT beams at a different power.
3. Switch off the MOT beam.
4. Release the atom by switching off the trapping beam for an interval of 0-100 μ s.
5. Recapture the atom by switching on the trapping beam.
6. Check the presence of the atom by illuminating with the MOT beams. If the atom is present, we repeat from step 2; else, we return to MOT formation to load another atom.

For a set of 11 different release intervals, we repeat each experiment several hundred times to obtain an estimate of the recapture probability. To extract the temperature, we find the best fit to the set of recapture probabilities generated by the Monte Carlo simulation for a range of temperatures (Fig. 3.6). For fair comparison, we set the maximum recapture probability of the simulation to our experimental figure of 0.987. The error of the temperature estimate is obtained by statistical method of bootstrapping. We resample a total of 4000 sets of recapture probabilities from the distribution of measured recapture probabilities. Fitting each of the new datasets to the Monte Carlo simulation, we obtain a distribution of temperature estimate (Fig. 3.7). We extract the error of the temperature estimate from the standard deviation of the distribution.

3.2. Experimental realisation

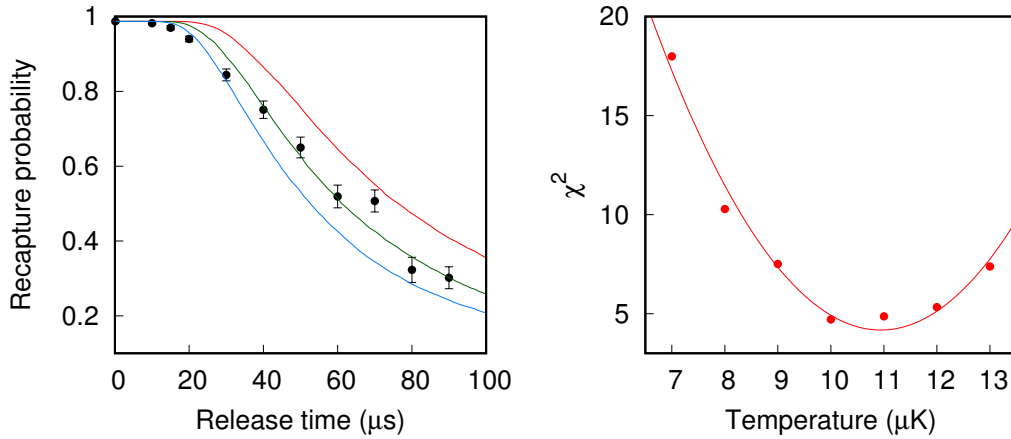


Fig. 3.6 An exemplary result of a release and recapture measurement. (Left) Comparison of atom recapture probabilities to the Monte Carlo simulation for atoms at 7 μK (blue), 10 μK (green), and 13 μK (red). Error bars represent standard error from binomial statistics. (Right) Extracted χ^2 from the fit to the Monte Carlo simulation for atoms of various temperatures. Solid line is a fit to a parabola.

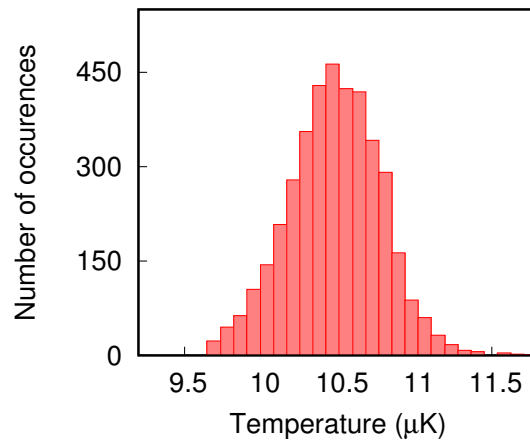


Fig. 3.7 A distribution of temperature estimate obtained from bootstrapping with data in Fig 3.6. A total of 4000 sets of recapture probabilities are sampled from the measured distribution and then fit to the Monte Carlo simulation.

3.3. PGC dependence on trap polarization

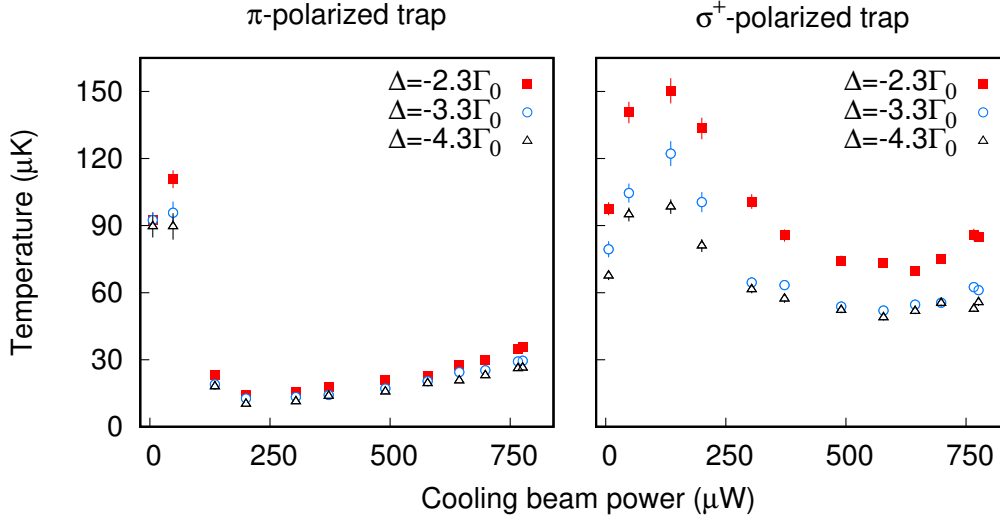


Fig. 3.8 Temperature of the atoms after PGC over the total cooling beam power in B_1 , B_2 , and B_3 . Error bars represent statistical uncertainty (one standard deviation). Systematic uncertainties, caused by errors in the determination of trap frequencies and the beam waist, are smaller than the statistical uncertainties.

3.3 PGC dependence on trap polarization

3.3.1 Linearly and circularly polarized trap

First, we compare PGC in a linearly π -polarized (parallel to beam B_3 , see Fig. 3.1) trap with that in a circularly σ^+ -polarized trap. To optimise the cooling parameters for each trap configuration, we adjust the cooling beam power and frequency. While the total power is varied, the ratio of power in the cooling beams is kept fixed with twice amount of power in B_3 than in B_1 and B_2 .³ The cooling beam frequency is altered from $2\Gamma_0$ to $4\Gamma_0$ red-detuned from the natural transition frequency.

Figure 3.8 shows the temperature of the atoms after PGC for the respective cooling parameters. The lowest temperature is achieved in the π -polarized trap at $10.3(3) \mu\text{K}$, which is approximately 5 times lower than the lowest temperature observed in the σ^+ -polarized trap at $49(1) \mu\text{K}$. We observe the typical PGC behaviour of lower temperatures for larger detunings of the cooling beam and an optimal cooling power below which the temperature increases sharply [113, 114]. This behaviour is more pronounced in the π -polarized trap than in the σ^+ -polarized trap.

³While having more power in B_3 than in B_1 and B_2 increases the lifetime of the atom in a circularly polarized dipole trap (see Section 2.6.3), we observe no significant difference in both the lifetime and the temperature of the atom by varying this ratio from 4.5 to 2.

3.3. PGC dependence on trap polarization

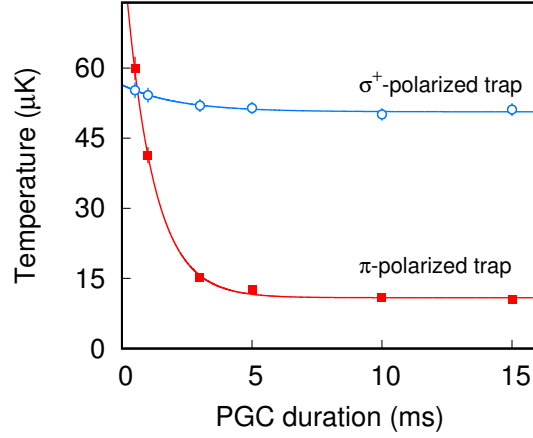


Fig. 3.9 Temperature of the atoms after PGC for a varying cooling duration. Optimal cooling beam power is used respectively for both the π -polarized trap (red square) and the σ^+ -polarized trap (blue circle). Solid lines are fits to exponentials. Error bars represent one standard deviation.

Subsequently, the cooling beam power and frequency are set to reach the lowest temperature for each trap configuration. Figure 3.9 shows the temperature of the atoms after a variable duration of PGC. In the π -polarized trap, the atom is quickly cooled to the lowest temperature with a $1/e$ -time constant of $1.1(1)$ ms; whereas in the σ^+ -polarized trap, PGC is inhibited and the atom remains close to the initial temperature.

3.3.2 Imperfect linearly polarized trap

We further test the sensitivity of the cooling in the π -polarized trap to imperfections of the trap polarization. The quality of the polarization here is quantified as the polarization extinction ratio

$$\varepsilon = 10 \text{ dB} \log_{10}(P_{\max}/P_{\min}), \quad (3.5)$$

where P_{\max} and P_{\min} are the maximum and minimum transmitted power through a rotating film-polarizer (Thorlabs LPVIS100, $\varepsilon > 50$ dB). Figure 3.10 shows the temperature of atoms after PGC as we deliberately introduce a slight ellipticity to the trap polarization. We find a high sensitivity of the cooling to the purity of the linear polarization. Already at $\varepsilon = 32$ dB, the temperature increases to $12.8(4)$ μK , which is notably higher compared to the lowest temperature of $10.3(3)$ μK achieved at $\varepsilon = 35$ dB. We do not expect much lower temperatures for polarization extinction

3.3. PGC dependence on trap polarization

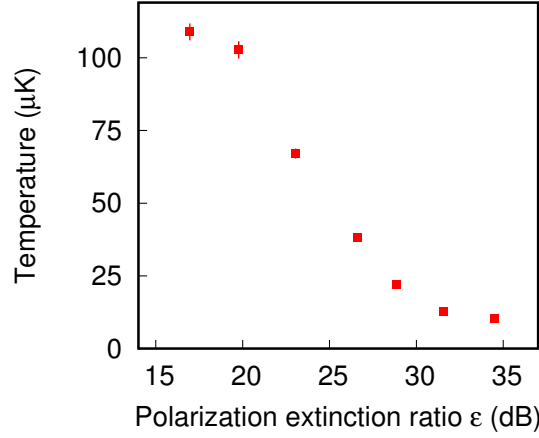


Fig. 3.10 Temperature of the atoms after PGC in a π -polarized trap depending on the polarization extinction ratio. The cooling beam power is optimised for the highest value of ϵ . Error bars represent one standard deviation.

ratios above $\epsilon = 35$ dB because for our lowest observed temperature of $10.3(3) \mu\text{K}$, the mean phonon number of the radial mode $\bar{n}_r = (e^{\hbar\omega_r/k_B T} - 1)^{-1} = 1.5(1)$ is close to the theoretical limit of $\bar{n} \approx 1$ [115, 116]. Recently, a similar value for the mean phonon number has also been observed for PGC of trapped ions [117]. We note that the inefficient PGC due to imperfections of the trap linear polarization can be overcome by applying a suitable magnetic field [93, 94].

3.3.3 Switching trap polarization after PGC

In our experiments to probe light-atom interaction, we drive the closed transition $5^2S_{1/2}, F = 2, m_F = -2 \rightarrow 5^2P_{3/2}, F' = 3, m_F = -3$ with a σ^- -polarized probe that is co-propagating with the FORT along z axis. A π -polarized trap parallel to x axis results in state mixing in the excited state manifold $5^2P_{3/2}, F' = 3$ along z axis. In this case, the σ^- -polarized probe propagating along the z axis cannot efficiently drive the $5^2S_{1/2}, F = 2, m_F = -2 \rightarrow 5^2P_{3/2}, F' = 3, m_F = -3$ transition. To efficiently address that transition, we operate the trap in a circular polarization, which unfortunately inhibits PGC. Therefore, we attempt to combine the best of both by first performing PGC in a π -polarized trap before conducting the experiment in a σ^+ -polarized trap via dynamical control of the trap polarization.

The polarization switch is implemented with a free-space transverse electro-optical polarization modulator (Newport 4102NF). Insertion of the polarization modulator and additional waveplates compromises the purity of the π -polarization

and reduces the polarization extinction ratio to $\varepsilon = 33$ dB. As a result, we find a slightly increased temperature of $13.0(4) \mu\text{K}$ after PGC in the π -polarized trap. We then perform PGC with the trap in π -polarization, switch to σ^+ -polarization, and momentarily pause for 1 ms before conducting the release recapture experiment. In this configuration, we observe a marginally increased temperature of $13.6(3) \mu\text{K}$, which is likely due to the approximate 1% change in power of the trapping beam after switching. Nevertheless, the achieved temperature is a significant improvement over PGC in a σ^+ -polarized trap, which at best reaches $49 \mu\text{K}$, and thus demonstrates the technical feasibility of switching the trap polarization *in situ*.

3.4 Summary

We demonstrated that σ^+ - σ^- polarization gradient cooling in a linearly polarized dipole trap leads to a lower atom temperature compared to a circularly polarized trap [58]. The cooling limit shows a strong sensitivity on the purity of the linear polarization of the trap; we measure a temperature increase from $10.3(3) \mu\text{K}$ to $12.8(4) \mu\text{K}$ as the polarization extinction ratio is reduced from 35 dB to 32 dB.

In a way, our results agree with the review article [81], published almost two decades ago, stating ‘... linearly polarized light is usually the right choice for a dipole trap...’. However, in practice the choice of the trap polarization is often set for other reasons than to optimise the PGC. For example, in our experiment to test light-atom interaction with co-propagating FORT and probe light, a circularly polarized trap is necessary to efficiently drive the strong cycling transition. Thus, we further showed that switching the trap polarization from linear to circular after PGC induces only minor heating, resulting in lowest atom temperatures of $13.6(3) \mu\text{K}$. The dynamical control of the trap polarization is employed in the subsequent experiments, and is thus foundational to the methodology of this thesis.

Chapter 4

Quantifying free-space light-atom interaction

This chapter presents the characterisation of the light-atom coupling efficiency for our setup. We employ two methods, a transmission measurement and a saturation measurement. Lastly, we experimentally investigate the reduction of light-atom coupling due to atomic motion. A simple model is devised and compared to our observation. The findings of this chapter have been published in [59]¹.

4.1 Transmission measurement

In this section, we present a transmission (extinction) measurement to determine the light-atom coupling efficiency Λ (see Section 2.2.2 for definition). As the complete theoretical model which relates the amount of scattering or extinction to the coupling efficiency has been comprehensively described in Ref. [39, 61, 62], we only introduce the key concept here. We note that a derivation based on the quantum input-output formalism arrives at the same results [118, 119].

4.1.1 Basic idea

Let us consider a simple transmission setup with an atom at the joint focus of two lenses as shown in Fig. 4.1. The probe beam originates from a collimated output of a single mode fibre and is focused onto the atom through lens L_1 . The opposing lens L_2 re-collimates the probe beam, which is then coupled into a single mode fibre.

¹Y.-S.C. and M.S. performed the experiments and analysed the data. C.K. conceived and supervised the project. All authors discussed the results and wrote the paper.

4.1. Transmission measurement

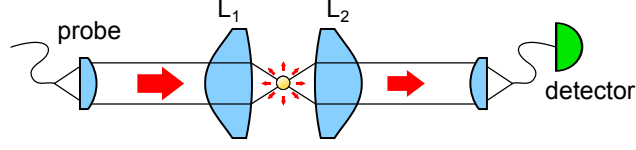


Fig. 4.1 Simplified optical setup for a transmission measurement. $L_{1(2)}$: lens.

The total electric field \vec{E}' of the light moving away from the atom is a superposition of the probe field \vec{E}_p and the field scattered by the atom \vec{E}_{sc} [39]:

$$\vec{E}' = \vec{E}_p + \vec{E}_{sc}. \quad (4.1)$$

In the case of driving a two level transition with a faint coherent probe beam, i.e., the power of the probe is way below saturation of the atomic transition, the amplitude of the scattered field

$$E_{sc} \propto -\frac{i\Gamma_0}{2\Delta + i\Gamma_0} E_p, \quad (4.2)$$

where Γ_0 is the natural linewidth of the atomic transition and Δ is the detuning from resonance. The negative sign here represents that the two fields accumulate a total relative phase shift of π from the contribution of a $\pi/2$ Gouy phase shift, and a $\pi/2$ phase shift of resonant scattering by the atom [120]. Therefore, the light field destructively interferes in the forward direction, which results in an extinction.

Projecting this light field onto a detector after a single-mode fibre, we obtain an electric field amplitude

$$E_f = \int \vec{E}'(\vec{r}) \vec{G}^*(\vec{r}) dS, \quad (4.3)$$

where $\vec{G}(\vec{r})$ with $\int \vec{G}(\vec{r}) \vec{G}^*(\vec{r}) dS = 1$ is the normalised collection mode, and dS is the differential area element perpendicular to the optical axis. In general for imperfect mode matching between the probe mode and the collection mode, E_f is a complex number. As such, the relative transmission τ , which is the optical power at detector normalised to the probe power $|\vec{E}_p|^2$, contains Lorentzian and dispersion-like terms [42],

$$\tau = \frac{|E_f|^2}{|\vec{E}_p|^2} \quad (4.4)$$

$$= 1 + A^2 \mathcal{L}(\Delta) + 2A \mathcal{L}(\Delta) \left[\Delta \sin \phi - \frac{\Gamma}{2} \cos \phi \right], \quad (4.5)$$

4.1. Transmission measurement

where

$$\mathcal{L}(\Delta) = \frac{1}{(\Delta^2 + \Gamma_0^2/4)} \quad (4.6)$$

is a Lorentzian profile, the coefficient A and the phase ϕ depend on the mode matching condition.

In the case of perfect mode matching between the probe mode and the collection mode, we can set the mode function as

$$\vec{G}(\vec{r}) = \frac{\vec{E}_p}{\sqrt{E_p}}, \quad (4.7)$$

which leads to the definition

$$E_p = \int \vec{E}_p(\vec{r}) \vec{G}^*(\vec{r}) dS. \quad (4.8)$$

The coefficients in Eq. (4.5) simplify to $A = \Gamma_0 \Lambda$ and $\phi = 0$, resulting in a transmission spectrum $\tau(\Delta)$ that is purely Lorentzian [53]. The resonant ($\Delta = 0$) scattered field amplitude is exactly $E_{sc} = -2\Lambda E_p$. The resonant transmission takes the well-known expression as [118]

$$\tau = (1 - 2\Lambda)^2, \quad (4.9)$$

and likewise the resonant extinction is

$$\varepsilon = 1 - \tau \quad (4.10)$$

$$= 4\Lambda(1 - \Lambda). \quad (4.11)$$

At $\Lambda = 0.5$, the probe results in a complete extinction $\varepsilon = 1$ in the forward direction and is thus fully reflected.

4.1.2 Experimental realisation

The complete experimental setup has been described in Chapter 2 and is shown in Fig. 2.1. Here, we perform a transmission measurement by probing the closed transition $5^2S_{1/2}, F = 2, m_F = -2 \rightarrow 5^2P_{3/2}, F' = 3, m_F = -3$ near 780 nm. The probe beam originates from the collimated output of a single mode fibre and has an approximately Gaussian beam profile with a beam waist of 2.7 mm before the lens. We set the power of the probe beam to contain on average 550 photons per pulse of 20 ms length, which is few orders of magnitude lower than the saturation power of the corresponding transition.

4.1. Transmission measurement

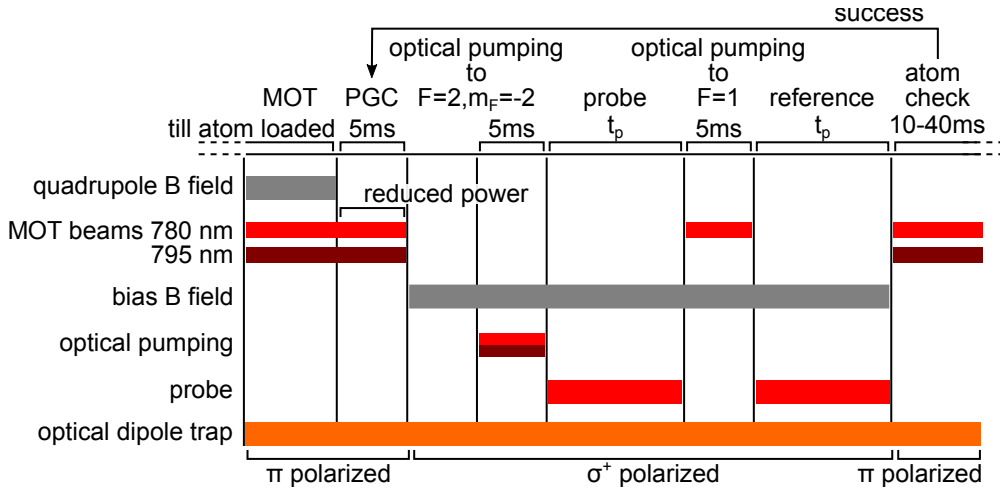


Fig. 4.2 Experimental sequence to probe the light-atom interaction.

Figure 4.2 depicts the experimental sequence. The experiment is triggered to begin upon the loading of a single ^{87}Rb atom from the magneto-optical trap (MOT) into a linearly π -polarized far-off-resonance optical dipole trap (FORT) and then proceeds as follows:

1. Turn off the quadrupole magnetic field to disperse the MOT cloud.
2. Perform polarization gradient cooling (PGC) for 5 ms. (see Chapter 3)
3. Apply a bias magnetic field of 0.74 mT along the optical axis and switch the FORT to circularly σ^+ -polarized.
4. Perform optical pumping for 5 ms into $5^2S_{1/2}, F = 2, m_F = -2$ state.
5. Probe for a duration $t_p = 20$ ms during which the detection events are recorded. (probe cycle)
6. Perform optical pumping for 5 ms into $5^2S_{1/2}, F = 1$ state to shift the atom out of resonance with with probe field by 6.8 GHz.
7. Repeat the probe for a duration $t_p = 20$ ms to determine the power as a reference measurement. The reference measurement is done immediately after the probe cycle to ensure a minimum discrepancy caused by power fluctuation of the probe. (reference cycle)
8. Check the presence of the atom by fluorescence scattering with the MOT beams. The bias magnetic field is turned off and the FORT is switched to π -polarized. If the atom is present, we consider the data to be valid and repeat

4.1. Transmission measurement

from step 1; otherwise, the data is discarded and we return to MOT formation to load another atom.

To acquire sufficient statistics, we repeat this sequence over 4000 experimental cycles.

4.1.3 Results

The transmission is computed from the ratio of the total detected photons during the probe cycle, N_{probe} , and reference cycle, N_{ref} , as

$$\tau = \frac{N_{\text{probe}}}{N_{\text{ref}}}, \quad (4.12)$$

with a background correction of 155 counts per second. Tuning the frequency of the probe field, we obtain a transmission spectrum as shown in Fig. 4.3 and determine a resonant extinction $\varepsilon = 17.7(1)\%$. The observed transmission spectrum shows approximately a Lorentzian profile but with a small deviation. This deviation is caused by the imperfect mode overlap between probe and collection mode. We infer a mode overlap of approximately 70% from the measured probe power, corrected for losses of the optical elements.

To account for the small deviation from imperfect mode matching, we include the phase ϕ as a free fit parameter following the model in Eq. (4.5),

$$\tau = 1 + (\Gamma\Lambda)^2 \mathcal{L}(\Delta) + 2\Gamma\Lambda \mathcal{L}(\Delta) \left[\Delta \sin \phi - \frac{\Gamma}{2} \cos \phi \right], \quad (4.13)$$

where the detuning from resonance frequency is

$$\Delta = \omega_p - \omega_0 - \delta\omega, \quad (4.14)$$

with ω_p as the probe frequency, ω_0 the natural transition frequency, and $\delta\omega = \omega_z + \omega_{\text{ac}}$ the frequency shift due to a Zeeman shift ω_z and an AC Stark shift ω_{ac} . Thus, we fit to Eq. (4.13) with four free parameters ($\chi_{\text{red}}^2 = 1.01$): coupling efficiency $\Lambda = 4.67(2)\%$, phase $\phi = 0.13(1)$ rad, frequency shift $\delta\omega = 48.03(3)$ MHz, and linewidth $\Gamma/2\pi = 6.9(1)$ MHz. Fitting to a Lorentzian model instead results in a χ_{red}^2 of 9.1.

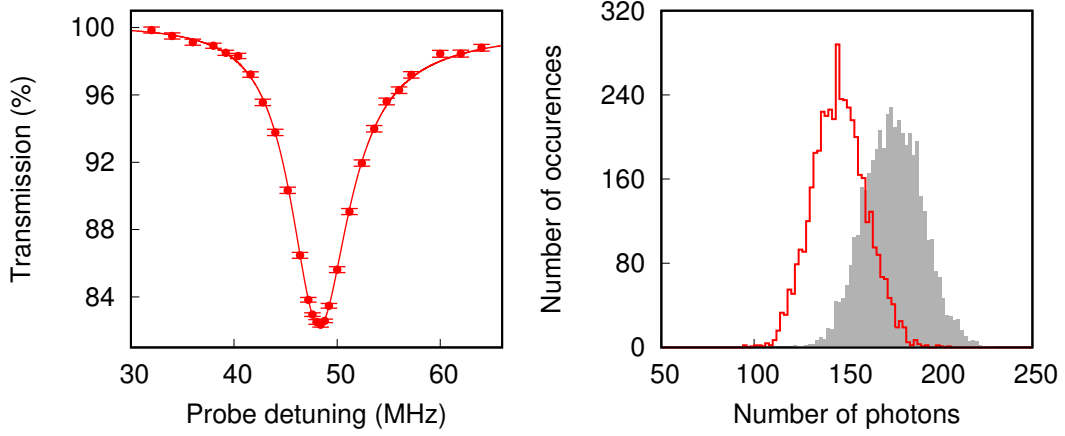


Fig. 4.3 Extinction of a weak coherent probe beam. (Left) Transmission spectrum. Solid line is a fit to Eq. (4.5) with free parameters: coupling efficiency $\Lambda = 4.67(2)\%$, phase $\phi = 0.13(1)$ rad, frequency shift $\delta\omega = 48.03(3)$ MHz, and linewidth $\Gamma/2\pi = 6.9(1)$ MHz ($\chi_{\text{red}}^2 = 1.01$), resulting in a resonant extinction of $\varepsilon = 17.7(1)\%$. Error bars represent one standard deviation due to propagated Poissonian counting uncertainties. (Right) Histogram of detected photons during the probe cycle (red) and reference cycle (grey) for the resonant data point.

4.2 Saturation measurement

In the following section, we present a saturation measurement to determine the coupling efficiency Λ as an alternative to the transmission measurement. While both methods supposedly produce identical outcomes, it has never been experimentally demonstrated.

4.2.1 Basic idea

The description here follows closely Ref. [51]. The incident power needed to saturate a target transition is a direct measurement of Λ . By saturation, we refer to saturation parameter $S=1$, for which the excited state population ρ in the steady state solution,

$$\rho = \frac{S}{2(S+1)} = \frac{1}{4}. \quad (4.15)$$

For a resonantly driven two level system, the saturation power P_{sat} is given by

$$P_{\text{sat}} = \frac{\hbar\omega_0\Gamma_0}{8} \frac{1}{\Lambda}, \quad (4.16)$$

4.2. Saturation measurement

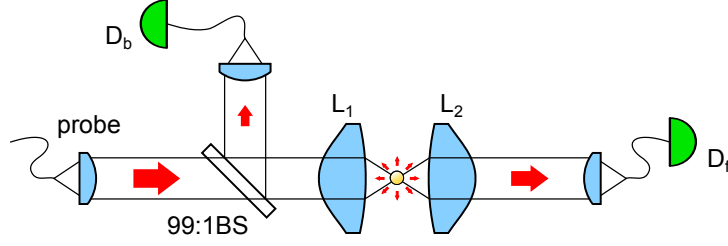


Fig. 4.4 Simplified optical setup for a reflection saturation measurement. $D_{b(f)}$: avalanche photodiode; BS: beam splitter; $L_{1(2)}$: lens.

where ω_0 is the transition frequency and Γ_0 is the natural linewidth. Thus, comparing the theoretical $P_{\text{sat},\Lambda=1}$ to the experimentally determined P_{sat} , we obtain

$$\Lambda = \frac{P_{\text{sat}}}{P_{\text{sat},\Lambda=1}}. \quad (4.17)$$

For our considered transition, the theoretical value of $P_{\text{sat},\Lambda=1} = 1.21$ pW.

To perform this measurement, we consider a setup as shown in Fig. 4.4. The atomic fluorescence rate R_b determined at the backward detector D_b is expected to follow a saturation function,

$$R_b = \frac{\eta\Gamma}{2} \frac{P_{\text{inc}}}{P_{\text{inc}} + P_{\text{sat}}}, \quad (4.18)$$

where η is the total detection efficiency and P_{inc} is the power of the incident beam at the position of the atom. In this configuration, the forward detector D_f can be used to measure P_{inc} .

4.2.2 Experimental realisation

The experimental sequence is identical to the one described in Section 4.1.2 with only differences in probe power and duration. During the probe cycle, we measure the backscattered photons using detector D_b , whereby during the reference cycle the detection events are recorded using the detector D_f . The number of detected photons in D_f after accounting for total detection efficiency η'_f is used to determine the incident power P_{inc} on the atom. We determine the detection efficiencies of D_b and D_f by comparing against a calibrated pin photodiode and a calibrated APD to $\eta_b = 59(3)\%$ and $\eta_f = 56(4)\%$, respectively. The total detection efficiency in D_f is

4.2. Saturation measurement

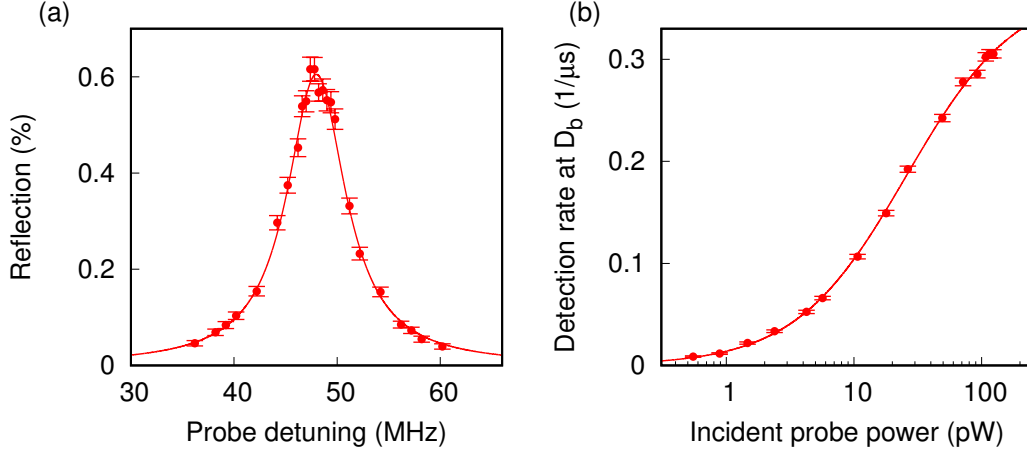


Fig. 4.5 (a) Light scattered into the backward detector D_b for different probe frequencies. The solid line is a Lorentzian fit of Eq. (4.22) with free parameters linewidth $\Gamma/2\pi = 6.9(1)$ MHz, frequency shift $\delta\omega/2\pi = 48.0(1)$ MHz, and resonant backscattering probability $p_{b,0} = 0.61(1)\%$, with $\chi_{\text{red}}^2 = 1.03$. (b) Resonant saturation measurement, with the solid line representing the fit to Eq. (4.18) with saturation power $P_{\text{sat}} = 26(2)$ pW and total detection efficiency $\eta = 1.95(2)\%$ as free parameters ($\chi_{\text{red}}^2 = 1.3$). Error bars represent one standard deviation due to propagated Poissonian counting uncertainties.

thus

$$\eta'_f = \underbrace{\eta_f}_{0.56} \times \underbrace{\text{fibre coupling}}_{0.62} \times \underbrace{\text{optical path}}_{0.9} \times \underbrace{\text{attenuation}}_{0.0049}. \quad (4.19)$$

The attenuation refers to a set of calibrated neutral density filters employed to avoid saturating the detector. From this we determine the incident power P_{inc} on the atom to be

$$P_{\text{inc}} = \frac{R_f}{\eta'_f} \hbar \omega_0, \quad (4.20)$$

where R_f is photon rate determined at D_f and ω_0 is the frequency of the photons. The experimental detection rates presented in the following are background-corrected for rates of 300 cps at detector D_b and 155 cps at detector D_f .

4.2.3 Results

Before proceeding to the saturation curve, we first measure a reflection spectrum to determine the resonance frequency. Tuning the frequency of the probe field ω_p , we fix the probe duration to $t_p = 20 \mu\text{s}$ and the power at about 4 pW. The probability p_b

4.2. Saturation measurement

for an incident photon to be backscattered by the atom is obtained by normalising the number of detected photons at detector D_b to the average number of incident photons during the probe interval [54, 120]. Accounting for detection losses, we obtain

$$p_b = \frac{N_b/\eta_b}{N_f/\eta_f'}, \quad (4.21)$$

where N_b and N_f are the number of total detected photons in D_b and D_f , respectively. Figure 4.5(a) shows the probability p_b for an incident photon to be backscattered by an atom when tuning the frequency ω_p of the probe field. The backscattering probability is proportional to the atomic excited state population and therefore follows a Lorentzian profile

$$p_b = \frac{p_{b,0}}{4\Delta^2/\Gamma_0^2 + 1}, \quad (4.22)$$

where $p_{b,0}$ is the resonant backscattering probability, and Δ is the detuning from resonance frequency defined as

$$\Delta = \omega_p - \omega_0 - \delta\omega, \quad (4.23)$$

with ω_p as the probe frequency, ω_0 the natural transition frequency, and $\delta\omega = \omega_z + \omega_{ac}$ the frequency shift due to a Zeeman shift ω_z and an AC Stark shift ω_{ac} . The experimental values of p_b in Fig. 4.5(a) can be well described by this model, with a frequency shift $\delta\omega/2\pi = 48.0(1)$ MHz from the natural transition frequency, $p_{b,0} = 0.61(1)\%$, and $\Gamma'/2\pi = 6.9(1)$ MHz.

To perform the saturation measurement, we vary the incident probe power from about 1 to 100 pW on resonance. At the same time, the probe duration is lowered to 4 μ s to minimise the heating of the atom via photon recoil. Figure 4.5(b) shows the resulting saturation curve. Fitting the atomic fluorescence rate R_b to the Eq. (4.18), we obtain a saturation power of $P_{\text{sat}} = 26(2)$ pW and a total detection efficiency $\eta = 1.95(2)\%$. We further infer a collection efficiency $\eta_c = \eta/\eta_b = 3.3(3)\%$ into a single mode fibre, which is comparable to the highest efficiencies reported for free- space optics [121, 122]. Comparing P_{sat} to $P_{\text{sat},\Lambda=1}$ indicates a coupling $\Lambda = 4.7(4)\%$, in agreement with the transmission measurement which yields $\Lambda = 4.67(2)\%$. The uncertainty of the coupling efficiency is dominated by the uncertainty of the efficiency η_f of detector D_f .

4.3. Role of thermal motion on interaction

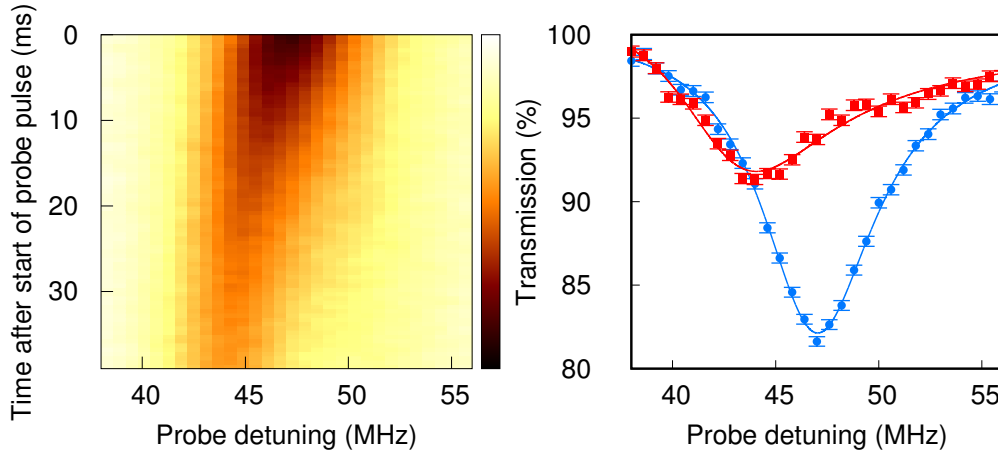


Fig. 4.6 Time-resolved transmission measurement. (Left) Each row presents a transmission spectrum similar to Fig. 4.3 and is obtained by collecting photodetection events in 0.5 ms wide time bins. (Right) Transmission spectrum at the beginning (blue) and the end (red) of the probe pulse extracted from the left plot. Solid lines are fits to Eq. (4.5). Error bars represent one standard deviation due to propagated Poissonian counting uncertainties.

4.3 Role of thermal motion on interaction

We have now characterised our light-atom interface to a coupling efficiency of $\Lambda = 4.7\%$. While the demonstrated light-atom interaction strength is 50% larger compared to our previous experiments with lenses of smaller numerical aperture (NA=0.55, [46]), the absolute coupling efficiency is still notably lower than the estimated upper bound of $\Lambda = 8.5\%$ (see Section 2.2.3). The residual temperature of the atom is commonly suspected to be a limiting factor in light-atom coupling [52, 39, 123]. Here, we experimentally investigate this issue by measuring the interaction strength at various atom temperatures.

As the recoil associated with the scattering of the probe field increases the kinetic energy of the atom, different atom temperatures can be accessed by following the temporal evolution of the probe transmission. Hence, we perform a transmission measurement identical to Section 4.1.2 with an extended probe duration to $t_p = 40$ ms, which contains on average about 9000 photons. We tune the probe frequency and time-tag the photodetection events during the probe interval. Sorting the events into 0.5 ms wide time bins, we obtain a time-resolved transmission spectrum as shown in Fig. 4.6. In the following, we present a simple model and compare it to our experimental observation.

4.3. Role of thermal motion on interaction

4.3.1 Model

The atomic thermal motion which leads to a finite positional spread affects the light-atom coupling in two ways: First, it reduces the coupling directly because the atom does not coincide precisely with the probe focus, but instead averages over its intensity distribution [123]. Secondly, the frequency of the atomic transition is lowered as the atom averages over the intensity distribution of the dipole trap.

We model the temperature dependent transmission spectrum by including also the spatial dependence in the frequency shift $\delta\omega(\vec{r}) = \omega_z + \omega_{\text{ac}}(\vec{r})$ and the mode overlap $\Lambda(\vec{r})$ [123] in Eq. (4.13), where \vec{r} is the position of the atom relative to the centre of the trap. Given the large beam waist $w_0 = 1.4\ \mu\text{m}$ of the dipole trap, the AC Stark shift $\omega_{\text{ac}}(\vec{r})$ is treated in the paraxial approximation,

$$\omega_{\text{ac}}(\vec{r}) = \omega_{\text{ac}} \left[\frac{w_0}{w(z)} \right]^2 \exp \left[\frac{-2r^2}{w(z)^2} \right], \quad (4.24)$$

where $\omega_{\text{ac}} = 57.6\ \text{MHz}$ is the AC Stark shift for an atom localised at the focus. We further define an effective coupling efficiency

$$\Lambda_{\text{eff}}(\vec{r}) = (1 - \alpha) \Lambda(\vec{r}), \quad (4.25)$$

where we evaluate the spatial dependence of the coupling efficiency $\Lambda(\vec{r})$ according to [39], which includes the changes of the local electric field polarization of the probe light near the focus. The parameter α is heuristically introduced to account for a reduced interaction strength due to experimental imperfections such as optical aberration.

The transmission spectrum, averaged over many different spatial configurations, is then given by

$$\langle \tau \rangle = \int p(T, \vec{r}) \tau(\vec{r}) d^3r, \quad (4.26)$$

where $p(T, \vec{r})$ is the probability distribution of the atom position. We treat the motion of the atom classically and assume that the probability distribution $p(T, \vec{r})$ is governed by a Maxwell-Boltzmann distribution with standard deviations of the positional spread of the atom

$$\sigma_i = \sqrt{\frac{k_{\text{B}} T}{m \omega_i^2}}, \quad (4.27)$$

where k_{b} is the Boltzmann constant, T the temperature, m the mass of ^{87}Rb , and ω_i the trap frequencies with $i = x, y, z$. For this experiment, the trap frequencies are mea-

4.3. Role of thermal motion on interaction

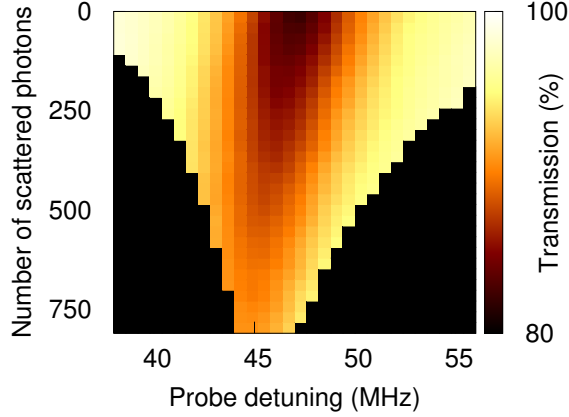


Fig. 4.7 Reorganised time-resolved transmission spectrum (Fig. 4.6) from probe duration into number of scattered photons according to Eq. (4.28). Black regions of the plot represent null data points that do not have any recorded events.

sured to be $\omega_x/2\pi = 107(1)$ kHz, $\omega_y/2\pi = 124(1)$ kHz, and $\omega_z/2\pi = 13.8(1)$ kHz, respectively. Equation (4.26) can then be evaluated by a Monte-Carlo method. Each scattered photon increases the total energy of the atom by $2E_r$, where $E_r = \hbar^2 k^2 / 2m$ is the photon recoil energy. The gained energy is anisotropically distributed because of the uni-directional excitation by the probe beam. Each photon leads therefore, on average, to an energy increase of $\frac{2}{3}E_r$ in the radial directions, and $\frac{4}{3}E_r$ in the axial direction. From a release-recapture technique [97], we infer an initial atom temperature of $21(1)$ μK (see Section 3.2.2). Thus, after 500 scattering events the axial temperature is increased by approximately 120 μK to just below Doppler temperature $T_D = 146$ μK .

4.3.2 Results

Extracting the temperature dependency of the light-atom interaction directly from the time-resolved transmission spectrum is difficult because the scattering rate and therefore the motional heating vary during the probe interval and depend on the probe frequency. For a quantitative analysis, we sort the detection events for each probe frequency according to the number of scattered photons instead of the probe pulse duration. The number of scattered photons $N_{\text{sc}}(t)$, time-integrated from the beginning of the probe interval to time t , is calculated from the transmitted photons via

$$N_{\text{sc}}(t) = \sum_{t_i=0}^t [N_{\text{ref}}(t_i) - N_{\text{probe}}(t_i)] / \eta_f \eta_{\text{op}}, \quad (4.28)$$

4.3. Role of thermal motion on interaction

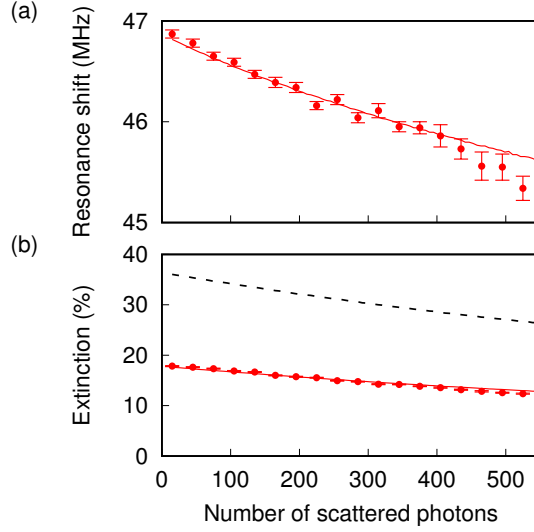


Fig. 4.8 The effect of recoil heating on the resonance frequency (a) and extinction (b) obtained from Fig. 4.7. (a) Solid red line is the numerical result of Eq. (4.26) with the frequency shift at the centre of trap $\delta\omega(0)$ as a free fit parameter ($\chi_{\text{red}}^2 = 1.4$). (b) The temperature dependence of extinction is well reproduced by Eq. (4.26) with $\alpha = 0.54(1)$ as a free fit parameter (red solid line, $\chi_{\text{red}}^2 = 11.6$). Dashed black line is the expected extinction for an ideal lens, given by Eq. (4.26), with $\alpha = 0$. Error bars represent one standard deviation obtained from least-squares fit of the individual spectra.

where $N_{\text{ref}}(t_i)$ and $N_{\text{probe}}(t_i)$ are the numbers of detected photons at detector D_f in time bin t_i during the reference and the probe interval, respectively, $\eta_f = 56(4)\%$ the detection efficiency, and $\eta_{\text{op}} = 59(5)\%$ the optical path loss from the atom to the detector. We choose a relative bin width of 30 scattered photons and reorganise the detection events from Fig. 4.6 into Fig. 4.7. Subsequently, we extract the resonance frequency and the extinction by fitting to Eq. (4.5). The resonance frequency and the extinction decrease fairly linearly with the number of scattered photons (Fig. 4.8). After scattering approximately 500 photons, the resonance frequency is lowered by $1.5(1)$ MHz, and the extinction is reduced by approximately 30% to $\varepsilon = 12.4(1)\%$.

The frequency shift expected from Eq. (4.26) matches well with the experimental results [Fig. 4.8(a)], where we use only the frequency shift at the centre of the trap $\delta\omega(0) = 47.32(5)$ MHz as a free fit parameter. This good agreement indicates that the model captures the effect of the dipole trap well. The initial resonance frequency is slightly lower compared to the results in previous section because of a slightly lower dipole trap power. Figure 4.8(b) (solid red line) shows the theoretical

extinction expected from Eq. (4.26) with our focusing parameters using $\alpha = 0.54(1)$ as a free parameter. The reduction of the extinction as a function of scattered photon numbers is well reproduced by the model. From Eq. (4.26) with $\alpha = 0.54$, we extrapolate a coupling efficiency $\Lambda = 5.1\%$ for a stationary atom, which is approximately 10% larger than the interaction observed for our lowest atom temperatures. This estimation provides an upper bound for the temperature effect because our model treats the atomic motion classically, and therefore does not include the finite spread of the motional ground state. The large value of $\alpha = 0.54$ means we observe less interaction compared to the tight focusing theory outlined in [39]. This reduction is likely to be caused by imperfections of the focusing lens and deviations of the incident field from a Gaussian beam.

Finally, we discuss possible origins of the observed linewidth broadening to 6.9 MHz from the natural linewidth of 6.0 MHz (Fig. 4.3 and 4.5). Doppler and power broadening are negligible because of the low atomic temperature of $21(1) \mu\text{K}$ and the weak excitation field in both measurements $P_{\text{probe}} < 0.02P_{\text{sat}}$. We use Eq. (4.26) to estimate whether the broadening is caused by the thermal motion in the spatially varying trap potential. We find an expected linewidth of 6.3 MHz for $T = 21 \mu\text{K}$. To account for the residual linewidth broadening, we roughly estimate an additional 2.8 MHz broadening from other noise sources, which is unlikely to be only due to the linewidth of the probe laser. The exact underlying factor is unknown.

4.4 Summary

We demonstrated a coupling efficiency $\Lambda = 4.7(4)\%$ between an external probe mode and the atomic dipole mode [59]. The coupling efficiency was determined independently from two different measurements: (1) extinction $\varepsilon = 17.7(1)\%$ of a weak coherent probe, and (2) saturation power $P_{\text{sat}} = 26(2) \text{ pW}$.

We further showed that the light-atom interaction can be limited by the thermal motion of the atom even at sub-Doppler temperatures. There are two underlying mechanisms that limits the interaction: First, averaging over the intensity distribution of the tightly focused probe field directly reduces the coupling. Secondly, averaging over the intensity distribution of the optical dipole trap induces a spatially varying AC stark shift on the atom. Comparing to a simple model, we conclude that our lowest atom temperatures of $21(1) \mu\text{K}$ ² reduces the coupling by approximately

²The lowest atom temperatures of $13(1) \mu\text{K}$ presented in Chapter 3 has only been achieved after these measurements.

4.4. Summary

10%. Hence, further cooling to the motional ground state promises only a moderate improvement [93, 94].

Chapter 5

Nonlinear photon-atom coupling with 4Pi microscopy

This chapter presents our adaptation of a super-resolution imaging technique, 4Pi microscopy, to efficiently couple light to a single atom. First, we briefly introduce 4Pi microscopy and extend the discussion of the transmission measurement to determine the coupling efficiency in this configuration. We then present the experimental implementation and compare the results of 4Pi to one-sided illumination. Lastly, from a photon statistics measurement of the transmitted light, we demonstrate nonlinear photon-atom coupling with our system. This chapter contains a considerable amount of material from our published work in [60]¹.

5.1 Introduction

The term 4Pi microscopy [56] refers to a super-resolution imaging technique, which improves the axial resolution by approximately four times over the Abbe diffraction limit [55] achieved by a standard confocal microscope. This limitation is overcome by using two opposing lenses with coinciding focal points to increase the aperture of the microscope. We illustrate this idea in Fig. 5.1: the path of the incident beam is split, and the object is coherently illuminated by two counter-propagating parts of the field simultaneously. In this way almost the entire solid angle is covered, limited only by the numerical aperture of the focusing lenses. The term 4Pi thus refers to the conceptual full solid angle covered by the microscope. In what follows, we briefly

¹Y.-S.C. and M.S. performed the experiments and data analysis. M.S. and C.K. conceived the experiment. All authors discussed the result and wrote the paper.

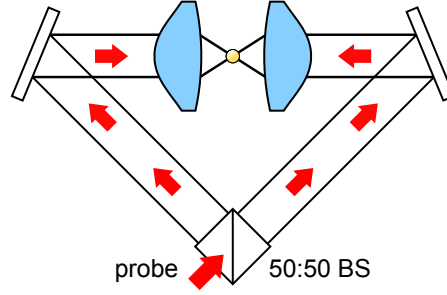


Fig. 5.1 Concept of a 4Pi illumination. The path of the probe beam is split, and the object is coherently illuminated by two counter-propagating parts of the field simultaneously. BS: beam splitter.

fit this idea into the context of light-atom interaction. We note that the possibility of 4Pi microscopy for light-atom coupling has been previously suggested [62, 124].

5.1.1 Transmission measurement in 4Pi configuration

In this section, we extend the discussion of the transmission measurement presented in Section 4.1 to the case of a 4Pi configuration to determine the light-atom coupling efficiency Λ (see Section 2.2.2 for definition). Specifically, we consider a resonant excitation and assume a perfect mode overlap between the probe and the collection mode.

Let us examine a 4Pi transmission setup with an atom at the joint focus of two lenses as shown in Fig. 5.2. The probe beam originates from a collimated output of a single mode fibre. It is split into path 1 and path 2 and focused onto the atom through lenses L_1 and L_2 , respectively. The opposing lens re-collimates the probe beam, which is then coupled via an asymmetric beam splitter into a single mode fibre connected to an avalanche photodetector, D_1 or D_2 , respectively. The total electric field of the light moving away from the atom is a superposition of the probe field and the field scattered by the atom [39]. We denote the respective electric field amplitudes at the detectors, i.e., after the projection onto the mode of the optical fibre, $E_{p,i}$ for the probe and $E_{sc,i}$ for the scattered field, with $i = 1, 2$ representing the paths. In the limit of weak excitation, the atom reacts to the parts of the probe field propagating in path 1 and 2 independently. Consequently, the scattered field consists of two contributions

$$E_{sc} = E_{sc,1} + E_{sc,2}. \quad (5.1)$$

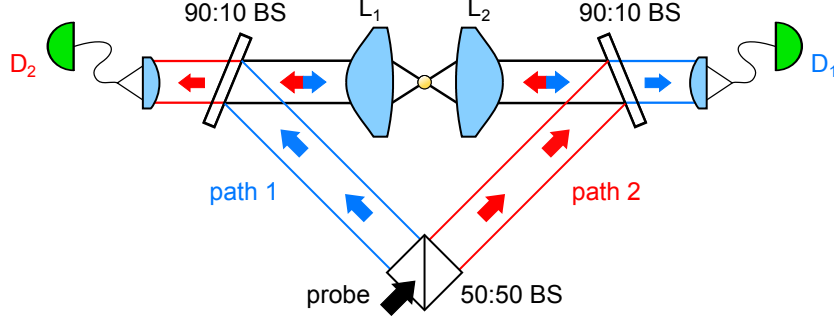


Fig. 5.2 Optical setup for a transmission measurement in a 4Pi configuration. The probe beam (black arrow) is split into path 1 (blue arrows) and path 2 (red arrows). The two beams then illuminate the atom from counter-propagating directions. Asymmetric beam splitters are used to sample the probe light after passing the atom. The probe light in path 1(2) is coupled into a single mode fibre connected to detector $D_{1(2)}$. By blocking one path, we recover the commonly employed one-sided illumination. BS: beam splitter, $L_{1(2)}$: high numerical aperture lens, $D_{1(2)}$: avalanche photodetector.

At detector D_1 , the total electric field is the sum of the transmitted probe field in path 1,

$$E_1 = E_{p,1} + E_{sc,1} + E_{sc,2}. \quad (5.2)$$

The scattered field contribution from path 1 projected onto the collection mode at D_1 is the same as one-sided illumination,

$$E_{sc,1} = -2\Lambda_1 E_{p,1}, \quad (5.3)$$

where Λ_1 is the light-atom coupling efficiency of path 1. On the other hand, the scattered field contribution from path 2 depends on the relative phase between the probe field in path 1 and path 2. Suppose the two counter-propagating probe fields have the same phase at the position of the atom, the scattered field contribution from path 2 projected onto the collection mode at D_1 is

$$E_{sc,2} = -2\sqrt{\Lambda_1\Lambda_2}E_{p,2}, \quad (5.4)$$

where Λ_2 is the light-atom coupling efficiency of path 2. Thus, the power at detector D_1 is given by

$$|E_1|^2 = |E_{p,1} - 2\Lambda_1 E_{p,1} - 2\sqrt{\Lambda_1\Lambda_2}E_{p,2}|^2. \quad (5.5)$$

Normalising to the input probe power, we obtain the individual transmission

$$\tau_1 = \frac{|E_1|^2}{|E_{p,1}|^2}. \quad (5.6)$$

For example, for one-sided illumination through lens L_1 , i.e., $|E_{p,2}|^2 = 0$, the transmission measured at detector D_1 recovers the expression as Eq. (4.9) [118],

$$\tau_1 = (1 - 2\Lambda_1)^2. \quad (5.7)$$

Similarly, the power at detector D_2 is obtained by exchanging subscripts 1 and 2.

In the 4Pi configuration, we determine the total coupling Λ_{total} from the total transmission

$$\tau_{\text{total}} = \frac{|E_1|^2 + |E_2|^2}{|E_{p,1}|^2 + |E_{p,2}|^2} \quad (5.8)$$

$$= (1 - 2\Lambda_{\text{total}})^2. \quad (5.9)$$

From Eq. (5.5), we find the power splitting given by the individual coupling,

$$|E_{p,2}|^2 = |E_{p,1}|^2 \Lambda_2 / \Lambda_1, \quad (5.10)$$

optimises the total coupling to $\Lambda_{\text{total}} = \Lambda_1 + \Lambda_2$. Therefore, for identical coupling $\Lambda_1 = \Lambda_2$, an even power splitting is optimal and doubles the coupling efficiency obtained from one-sided illumination.

In the experiment, we employ asymmetric beam splitters to switch between the 4Pi and one-sided illumination for ease of comparison under the same optical alignment. We note that using asymmetric beam splitters to sample individual transmission in path 1 and path 2 is not necessary to determine τ_{total} . For practical applications of 4Pi illumination, it is possible to probe directly the output port of the first 50:50 beam splitter and omit the asymmetric beam splitters to avoid photon loss.

5.1.2 Numerical simulation of electric field distribution

To obtain further insights, we numerically simulate the electric field distribution near the focal point for the case of 4Pi and one-sided illumination. We evaluate the electric field following exactly Section 3.2 of Ref. [39], which considers a Gaussian field resonantly driving a circularly polarized dipole transition near 780 nm, and

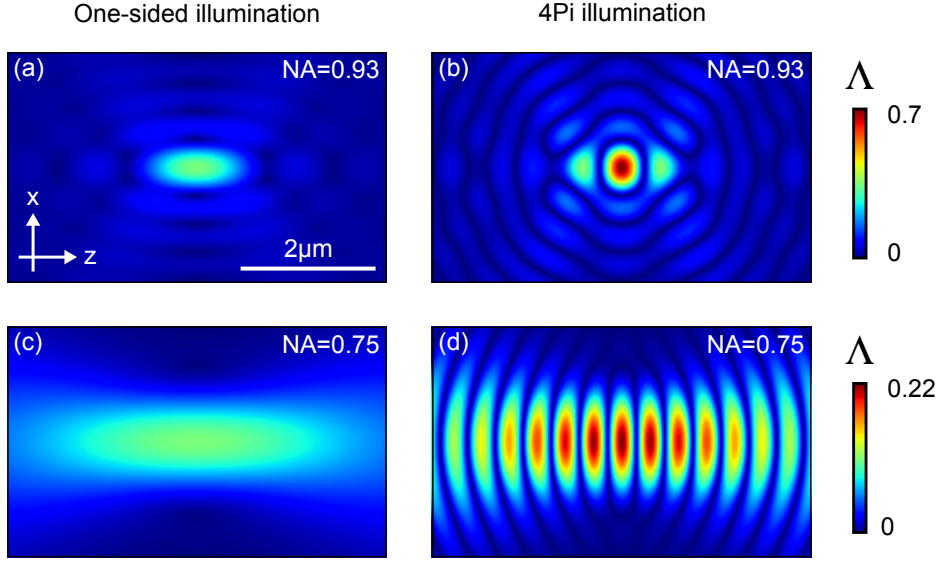


Fig. 5.3 Numerical results of the coupling efficiency Λ near the focal point. (a,b) Focusing parameters corresponding to an objective with numerical aperture $\text{NA}=0.93$ and an input beam waist which experiences less than 1% clipping losses from the aperture of the lens. (c,d) Focusing parameters used in this experiment ($\text{NA}=0.75$, input beam waist $w_0 = 2.7$ mm at lens, focal length $f = 5.95$ mm).

includes also the spatially varying polarization of the tightly focused probe light. In the case of 4Pi illumination, we assume that the field constructively interferes at the focal point. For clarity, we express the field distribution instead as the light-atom coupling efficiency Λ .

Figure 5.3 shows the results of the numerical simulation. To illustrate the full capability of 4Pi illumination, we first consider an objective of numerical aperture $\text{NA}=0.93$ with an input beam waist with less than 1% clipping loss [Fig. 5.3(b)]. As expected from 4Pi microscopy, the spatial distribution is greatly compressed in the axial direction. The resultant focus is a tightly localised volume, approximately a sphere of diameter $\lambda/2$ whereby the maximum mode overlap is doubled to 70% when compared to one-sided illumination.

Next, we evaluate with parameters specific to our experimental setup ($\text{NA}=0.75$, input beam waist $w_0 = 2.7$ mm, focal length $f = 5.95$ mm) [Fig. 5.3(d)]. The maximum mode overlap is similarly doubled in the 4Pi illumination. Notably, the spatial dependence exhibits a standing wave pattern with multiple antinodes of near maximum coupling and multiple nodes of zero coupling. Hence, to harness the advantage of the 4Pi technique, the atom is required to be precisely positioned in the axial

5.2. Experimental realisation

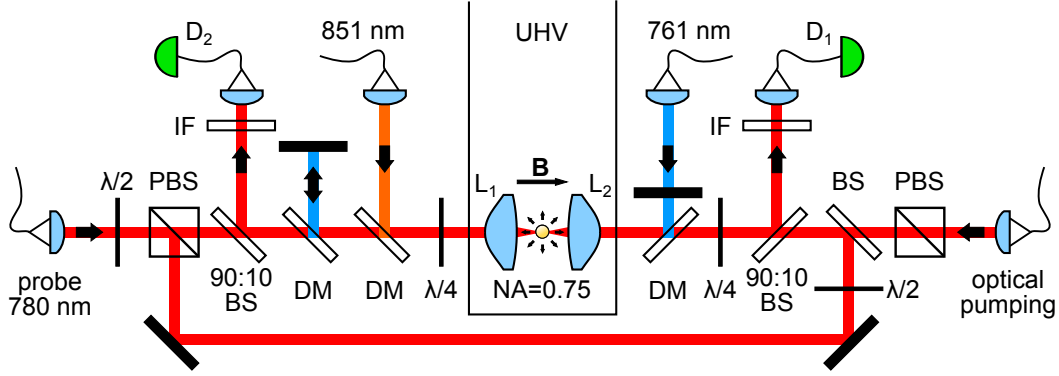


Fig. 5.4 Optical setup for probing light-atom interaction in a 4Pi configuration. D_1 , D_2 : avalanche photodetectors (APDs), IF: interference filter centred at 780 nm, $\lambda/2$: half-wave plate, $\lambda/4$: quarter-wave plate, (P)BS: (polarizing) beam splitter, DM: dichroic mirror, L_1 , L_2 : high numerical aperture aspheric lenses, \mathbf{B} : magnetic field, UHV: ultra-high vacuum chamber.

direction, specifically at an anti-node of the incident field even though we are not at the high numerical aperture limit.

5.2 Experimental realisation

5.2.1 Optical setup

Figure 5.4 shows the modified optical setup to adapt a 4Pi configuration. To control the power ratio of the probe in the two paths, we include a half-wave plate and a polarizing beam splitter.

From the numerical simulations earlier [Fig. 5.3(d)], we have learnt that the atom needs to be better confined along the axial direction in the 4Pi configuration. So we enhance the axial confinement with an additional blue-detuned standing wave dipole trap. The blue-detuned trap is formed by 761 nm linearly polarized light, has a trap depth of $U_0 \simeq k_B \times 0.1$ mK along the optical axis, and is overlapped with our primary dipole trap² (Fig. 5.5). The choice of blue-detuning avoids an additional light shift induced by the dipole trap to maintain similar experimental conditions for both 4Pi and one-sided illumination.

²The details of the primary dipole trap have been covered in Section 2.6.1. For this experiment, the trap is operated at a depth of $U_0 = k_B \times 1.88$ mK.

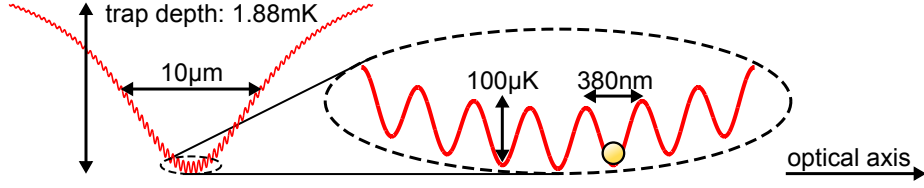


Fig. 5.5 A standing wave blue-detuned dipole trap at 761 nm is employed in conjunction with the primary red-detuned dipole trap at 851 nm to increase the spatial confinement along the optical axis.

5.2.2 Experimental sequence

We compare 4Pi and one-sided illumination by performing a transmission experiment with a weak coherent field driving the closed transition $5^2S_{1/2}, F = 2, m_F = -2 \rightarrow 5^2P_{3/2}, F' = 3, m_F = -3$ near 780 nm. The power of the probe field is well below the saturation power P_{sat} of the corresponding transition and is set to approximately $0.003P_{\text{sat}}$. The experimental sequence is generally the same as presented in Section 4.1.2 where we first introduced a transmission experiment.

To fully utilise the 4Pi arrangement, it is crucial to position the atom at an anti-node of the probe field. Unfortunately, the interference pattern of the probe field changes over time owing to slow drifts in the optical path lengths. The probe-atom coupling is further affected by similar drifts of the standing wave trap, and the probabilistic loading into particular positions. Here, we exploit the fact that once an atom is loaded, the timescale for a transmission experiment is much shorter (milliseconds) than the timescale of the drifts (>10 minutes). Therefore, the transmission is expected to be lowest when the atom is positioned at the anti-node of the probe field. In the following, we use the transmission as a signal to perform active phase stabilisation and postselection of the atom position.

5.2.3 Active phase stabilisation

For a full measurement over the duration of hours, it is possible for the probe and the trap standing wave patterns to drift out of phase. To avoid this scenario, we implement an active stabilisation scheme to keep the two patterns in phase. We use the transmission as a signal and minimise it by tuning the laser frequency of the blue-detuned standing wave trap over 100 MHz. Figure 5.6 shows the transmission over time with and without stabilisation. We initialise both measurements to the minimum transmission at the start. Without stabilisation, the transmission increases over time

5.2. Experimental realisation

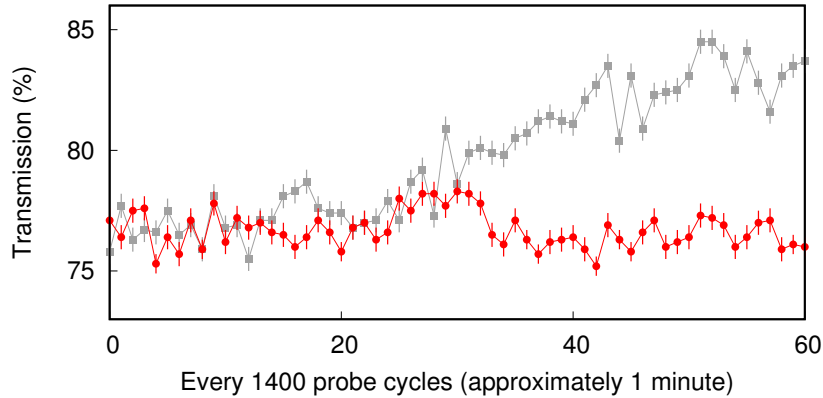


Fig. 5.6 Transmission of the probe with (red) and without (grey) active stabilisation. Each data point is an exact sum of 1400 measurement cycles, which takes about a minute to accumulate. Error bars represent one standard deviation of propagated Poissonian counting uncertainties.

as the two standing wave pattern drift out of phase; whereas with stabilisation, the transmission remains throughout. The stabilisation routine is performed every 16 minutes and takes 2 minutes to complete.

5.2.4 Postselection of the atom position

The phase stabilisation described in the previous section is tasked to handle long term interference pattern drifts. To solve the problem of shot-to-shot probabilistic atom loading into particular positions, we perform two independent transmission experiments in each sequence: one to check whether the atom is trapped at the right position and one to determine the light-atom interaction.

Figure 5.7(a) shows the experimental sequence. Splitting the probe and the reference cycles into two parts each of 1 ms, we separate them with a $4 \mu\text{s}$ pause. To minimise the effect of recoil heating from the probe field, the light-atom interaction experiment takes place before checking the atom position. So we tune the frequency of the first probe to measure the transmission spectra. The second probe cycle is used to check whether the atom has been trapped at an anti-node of the probe field. For this, the frequency of the probe field is set to be resonant with the atomic transition. Subsequently, we perform a reference measurement to obtain the instantaneous probe power.

Figure 5.7(b-d) illustrates the postselection procedure for which the probe field during the first probe cycle is resonant with the atomic transition. The position of

5.2. Experimental realisation

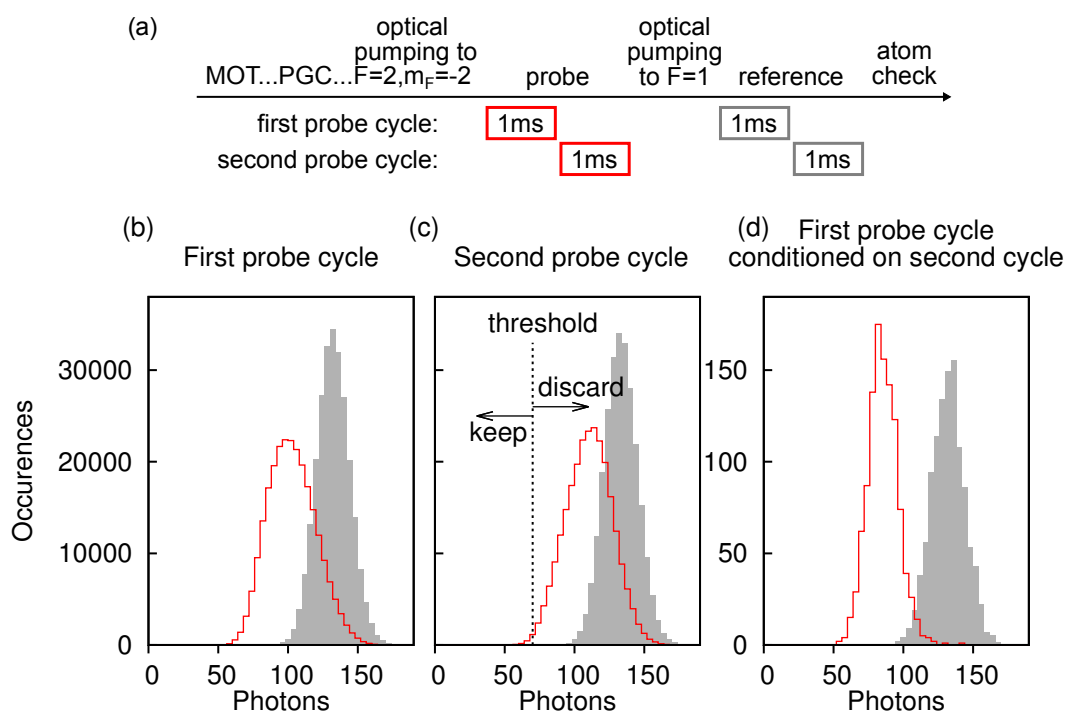


Fig. 5.7 (a) Simplified experimental sequence to illustrate the two probe cycles for postselection of the atom position. Refer to Fig. 4.2 for the complete sequence. (b-d) Photon counting histogram recorded during probe (red) and reference (grey) cycles. The total number of detected photons is the sum of events from detectors D_1 and D_2 . (b) First probe cycle for the case when the probe field is resonant to the atomic transition. (c) Second probe cycle. The dotted line marks the threshold for a postselection of approximately 0.5% of the total events. (d) Resultant events of the first probe cycle, conditioned on the second cycle using the marked threshold in (c).

5.3. Transmission experiment

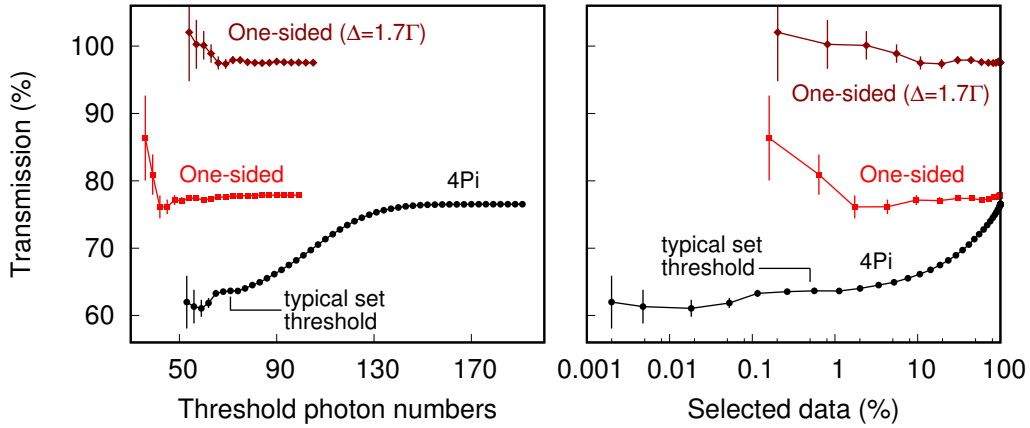


Fig. 5.8 Effect of the postselection procedure on the transmission for 4Pi and one-sided illumination. Left: Resonant transmission as a function of a postselection threshold value for 4Pi illumination (black circles) and one-sided illumination (red squares). The transmission values for one-sided illumination at a detuning $\Delta = 1.7\Gamma$ are also shown (dark red diamonds). The marked point indicates the threshold value that selects approximately 0.5% of the total events. Right: Same as left but as a function of selected data percentage. Error bars represent one standard deviation of propagated Poissonian counting uncertainties.

the atom is postselected based on the detected transmission during the second probe cycle. For an atom loaded into a desired site of the potential well, the transmission is low. Hence, we discard detection events in the first cycle if the number of photons detected in the second cycle is above a set threshold. Figure 5.8 shows the resultant transmission depending on the postselection threshold photon numbers. We use a threshold value that selects approximately 0.5% of the total events, trading off between data acquisition rate and selectivity of the atom position. This postselection procedure does not change the observed transmission for the case of one-sided illumination. For the upcoming transmission experiment, each data point takes about 15 to 30 minutes of measurement time.

5.3 Transmission experiment

5.3.1 Comparison between 4Pi and one-sided illumination

First, we perform the transmission experiment with one-sided illumination. Figure 5.9(a) shows the transmission spectrum of a weak coherent field, either probing via path 1 (blue) or path 2 (red). Comparing the resonant transmission $\tau_1 = 77.9(2)\%$

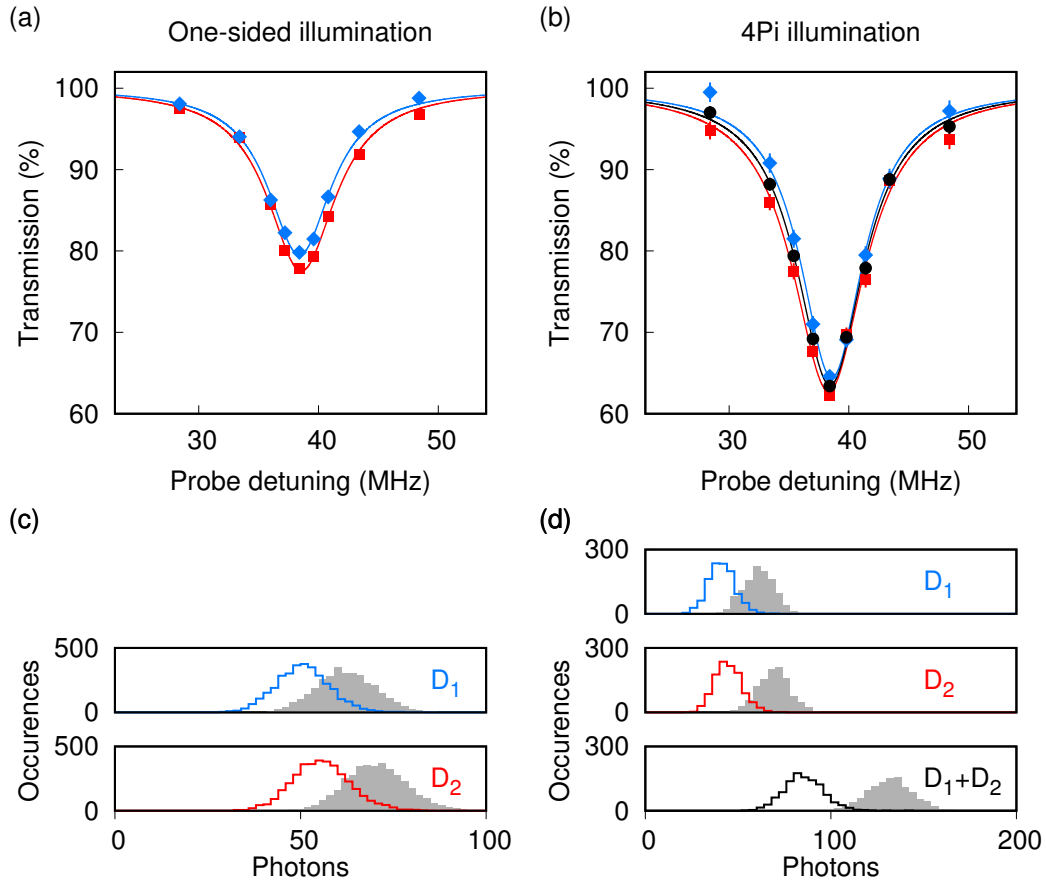


Fig. 5.9 Extinction of a weak coherent probe beam. (a) One-sided illumination via path 1 (blue diamonds) or path 2 (red squares). Solid lines are Lorentzian fits. (b) Same as (a) but with 4Pi illumination. The total transmission (black circles) is obtained from the sum of detectors D_1 and D_2 . Error bars represent one standard deviation of propagated Poissonian counting uncertainties. The FORT shifts the resonance frequency by approximately 38.5 MHz compared to the natural transition frequency. (c,d) Histogram of detected photons during the probe cycle (solid line) and reference cycle (grey) for the resonant data point of (a) and (b), respectively.

5.3. Transmission experiment

and $\tau_2 = 79.8(3)\%$ to Eq. (5.7), we find similar coupling efficiencies, $\Lambda_1 = 0.059(1)$ and $\Lambda_2 = 0.053(1)$ ³, as expected for our symmetric arrangement with two nominally identical lenses. Therefore, the maximum coupling expected in the 4Pi configuration is $\Lambda_{\text{total}} = \Lambda_1 + \Lambda_2 = 0.112(4)$, assuming perfect phase matching of the fields and ideal positioning of the atom.

We then proceed to illuminate the atom in the 4Pi arrangement with a near 50:50 power split. Scanning the probe frequency, we obtain transmission spectra as shown in Fig. 5.9(b). The increased light-atom coupling is evident from the strong reduction of transmission. The individual transmissions $\tau_1 = 62.3(5)\%$, $\tau_2 = 64.6(5)\%$, and the total transmission $\tau_{\text{total}} = 63.4(3)\%$ are significantly lower compared to the one-sided illumination. From the total transmission, we infer a total coupling of $\Lambda_{\text{total}} = 0.102(1)$, which is close to the theoretical prediction of 0.112(4).

5.3.2 4Pi illumination coupling dependence on power splitting

We next show that for a symmetric arrangement $\Lambda_1 \approx \Lambda_2$, the highest interaction in the 4Pi configuration is achieved with an equal power splitting $P_{2,\text{in}} \approx P_{1,\text{in}}$. Figure 5.10 displays the resonant transmissions for different relative beam powers in the two paths. For imbalanced beam powers, the total transmission is increased, albeit with a fairly weak dependence. In contrast, we find a strong dependence of the individual transmissions on the relative beam power. For example, at $P_{1,\text{in}} \approx 12P_{2,\text{in}}$, the total transmission is still low, $\tau_{\text{total}} = 71.2(8)\%$, but the two values for the individual transmissions are no longer equal: $\tau_{1,4\text{Pi}} = 74.0(8)\%$, $\tau_{2,4\text{Pi}} = 41(2)\%$. Figure 5.10 (solid lines) also shows that the observed behaviour of the transmission can be well reproduced by Eq. (5.5) without any free parameter. A closer look shows that the measured transmission values are slightly larger than expected from Eq. (5.5). This difference is likely due to the limited resolution of selecting the atom position and the thermal motion of the atom [59]. Though the values used in Eq. (5.5) from the one-sided illumination already include the thermal motion directly from the measurement, the effect is further enhanced in the 4Pi configuration. We are unable to quantify this effect as the process is coupled with the postselection of the atom position.

³In Chapter 4, we measured $\Lambda_2 = 4.7(4)\%$. The improvement to $\Lambda_2 = 5.3(1)\%$ here is mainly due to a better alignment of the probe beam, which is consequently granted by the need to simultaneously align both paths in the 4Pi configuration.

5.3. Transmission experiment

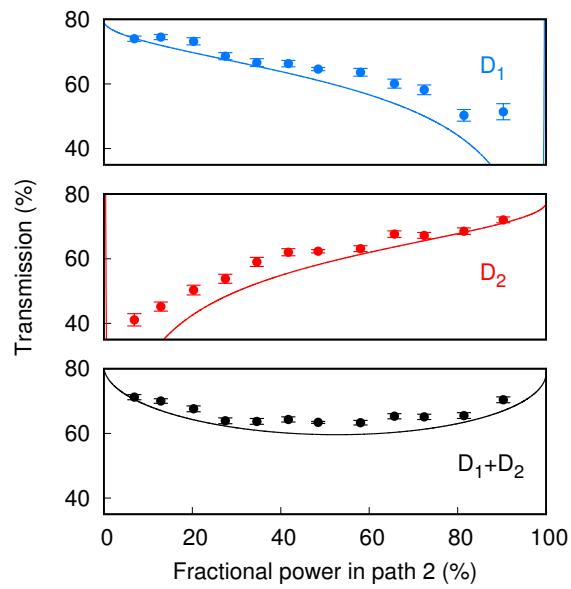


Fig. 5.10 Resonant transmission for different power splittings between path 1 and path 2. Transmission at detector D_1 (top), D_2 (centre) and the total transmission $D_1 + D_2$ (bottom). The total number of incident photons is kept constant. Solid lines are $\tau_{1(2)}$ and τ_{total} derived from Eq. (5.5), with Λ_1 and Λ_2 determined from one-sided illumination. Error bars represent one standard deviation of propagated Poissonian counting uncertainties.

5.4 Observation of nonlinear light-atom coupling

The nonlinear character of the photon-atom interaction can induce effective attractive or repulsive interactions between two photons [125–128]. These interactions can be observed as a modification of the photon statistics of the transmitted field if the initial field contains multi-photon contributions [129–133].

5.4.1 Photon statistics of transmitted light

A quantitative description of this effect has been developed in the context of waveguide quantum electrodynamics [134, 135]. For a weak coherent driving field, that is, ignoring contributions from number states with three or more photons, the second-order correlation function $g^{(2)}(\Delta t)$ takes the specific form

$$g^{(2)}(\Delta t) = e^{-\Gamma_0 \Delta t} \left(\left(\frac{2\Lambda}{1-2\Lambda} \right)^2 - e^{\frac{\Gamma_0 \Delta t}{2}} \right)^2, \quad (5.11)$$

where $\Gamma_0 = 2\pi \times 6.07 \text{ MHz}$ is the excited state linewidth. Figure 5.11 shows the dependence of photon statistics of transmitted light on the coupling efficiency. For $\Lambda = 0$, the transmitted light shows $g^{(2)}(0) = 1$ as expected for coherent laser light. For stronger light-atom coupling the changes of the photon statistics are more significant. Notably, for $\Lambda = 0.25$ the transmitted and the reflected light shows perfect anti-bunching, $g^{(2)}(0) = 0$, which signifies that the atom acts as a photon turnstile converting a coherent field completely into a single photon field. Photon bunching ($g^{(2)}(0) > 1$) for large values of Λ indicates an enhanced transmission probability when two photons are simultaneously incident; while one photon states are efficiently reflected, photon pairs saturate the atomic transition and have a larger transmission probability.

5.4.2 Measurement of second-order correlation function

We measure the second-order correlation function of the transmitted light using detector D_1 and D_2 as the two detectors of a Hanbury-Brown and Twiss setup [136]. By time-tagging the detection events at detector D_1 and D_2 during the probe phase, we obtain

$$g^{(2)}(\Delta t) = \frac{\langle p_1(t) p_2(t + \Delta t) \rangle}{(\langle p_1(t) \rangle \langle p_2(t + \Delta t) \rangle)}, \quad (5.12)$$

5.4. Observation of nonlinear light-atom coupling

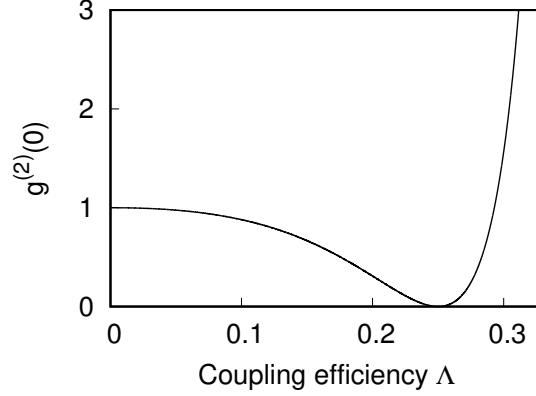


Fig. 5.11 Theoretical dependence of the second-order correlation function of the transmitted light following Eq. (5.11) for $\Delta t = 0$.

where $p_{1(2)}(t)$ is the detection probability at detector $D_{1(2)}$ at time t , and $\langle \rangle$ denotes the long time average. The photodetection events are sorted into a time delay histogram. To acquire the second-order correlation function, we accurately normalise this histogram to

$$r_1 \times r_2 \times t_{\text{bin}} \times T, \quad (5.13)$$

where $r_{1(2)}$ is the mean count rate at detector $D_{1(2)}$, t_{bin} the time bin width and T the total measurement time [137]. In order to make the normalisation robust against intensity drifts of the probe power and cycle-to-cycle variations of the light-atom coupling, we perform the normalisation for every 1 ms-long measurement cycle. Therefore, we obtain a normalised correlation function $g_i^{(2)}(\Delta t)$ (index i describes the measurement cycle) and then $g^{(2)}(\Delta t)$ from the weighted mean

$$g^{(2)}(\Delta t) = \frac{\sum_{i=1}^N g_i^{(2)}(\Delta t)(r_{1,i} + r_{2,i})}{\sum_{i=1}^N (r_{1,i} + r_{2,i})}. \quad (5.14)$$

To acquire sufficient statistics, we use 50% more photons in the probe pulse as compared to the transmission spectra in Fig. 5.9, and also relax the postselection criteria (Section 5.2.4) to select 10% of the experimental cycles thereby including atoms that are not optimally coupled to the probe field. Consequently, we measure an increased transmission $\tau_{\text{total}} = 70.3(3)\%$, and thus deduce a coupling $\Lambda_{\text{total}} = 0.0808(5)$ for this experiment. The correlations shown in the upcoming section are the result of approximately 200 hours of measurement time.

5.4. Observation of nonlinear light-atom coupling

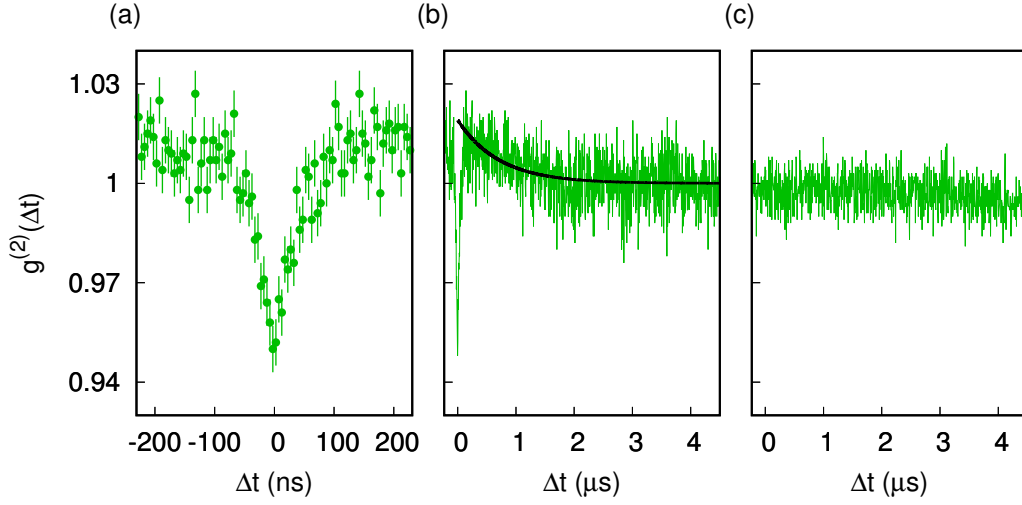


Fig. 5.12 Intensity correlation of transmitted light with a time bin width of 5 ns. Detector D_1 and D_2 are utilised as the two detectors of a Hanbury-Brown and Twiss setup, where time difference $\Delta t = t_1 - t_2$. (a) Computed from events during the probe cycle. (b) Same as (a) but with extended range. Solid line is a fit to Eq.(5.15). (c) Same as (b) but computed from events during the reference cycle in which the atom is not resonant with probe field. Error bars represent ± 1 standard error of mean.

5.4.3 Results and analysis

Figure 5.12(a,b) displays a clear signature of nonlinear photon-atom interaction in the intensity correlations of the transmitted light, observed in the form of photon anti-bunching at $\Delta t = 0$. For large Δt , the correlation disappears, and $g^{(2)}(\Delta t)$ approaches unity. No additional correlations are present in the transmitted light during the reference cycle in which the atom is not resonant with probe field [Fig. 5.12(c)].

Another notable feature is the super-Poissonian intensity correlation $g^{(2)}(\Delta t) > 1$ in range of $100 \text{ ns} < \Delta t < 1 \mu\text{s}$, visible in Fig. 5.12(b). Similar correlations have been observed in the fluorescence of single atoms in dipole traps induced by the atomic motion through the trap [138, 139]. Although the amplitude of the correlations is small, we nevertheless perform a deconvolution for a better comparison to Eq. (5.11). For diffusive motion the correlations are expected to decay exponentially, thus we fit

$$f(\Delta t) = 1 + A \exp\left(-\frac{\Delta t}{\tau_d}\right) \quad (5.15)$$

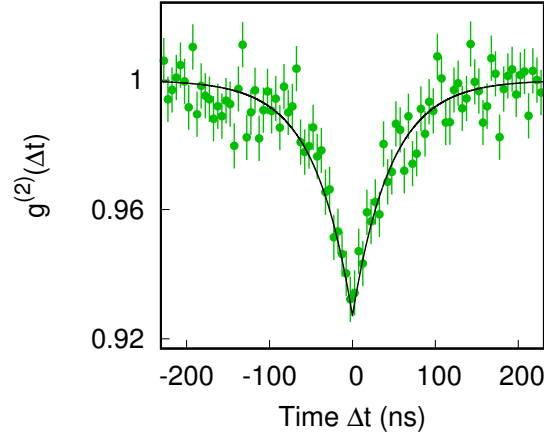


Fig. 5.13 Normalised second-order correlation function after deconvolution of the diffusive atomic motion. Solid line is the theoretical prediction of Eq. (5.11) from our measured coupling efficiency Λ without free parameter. Error bars represent ± 1 standard error of mean.

to $g^{(2)}(\Delta t)$, resulting in amplitude $A = 0.019(2)$, decay time constant $\tau_d = 0.71(8) \mu\text{s}$, with a reduced $\chi^2 = 1.07$ [Fig. 5.12(b), black solid line]. We note that the timescale τ_d of these correlations is much larger than the excited state lifetime $1/\Gamma_0 = 26.2 \text{ ns}$.

Figure 5.13 shows the resultant second-order correlation function after accounting for the small photon bunching effect ($\approx 1.7\%$) contributed by the diffusive atomic motion, i.e., after division by $f(\Delta t)$. The observed photon anti-bunching $g^{(2)}(0) = 0.934(7)$ is in good agreement with Eq. (5.11) without any free parameter.

5.5 Summary

In a 4Pi configuration, we demonstrated 36.6(3)% extinction of a weak coherent probe by a single atom, and thus a light-atom coupling efficiency $\Lambda = 10.2(1)\%$ [60]. The interaction strength is almost doubled when compared to one-sided illumination in which we measure $\Lambda_1 = 5.9(1)\%$ and $\Lambda_2 = 5.3(1)\%$ for either sides. Furthermore, we observed a modified photon statistics of the transmitted field in the form of photon anti-bunching $g^{(2)}(0) = 0.934(7)$. While the achieved nonlinearity of the interaction does not create strongly correlated photons yet, we showed that our free-space light-atom interface is nonlinear at the single photon level. Further work towards higher coupling efficiency at $\Lambda = 25\%$ may open path to a different single photon source, which operates on the nonlinear optical response of single atoms.

Chapter 6

Conclusion and Outlook

In this thesis, we described the development of a light-atom interface in free space. Our system with larger numerical aperture (NA=0.75) lenses compared to previous experiments [46, 118, 43] enabled us to investigate light-atom interaction at a tighter focusing geometry.

First, we examined the effect of atomic thermal motion on the interaction. We determined a light-atom coupling efficiency $\Lambda = 4.7(4)\%$ between an external probe mode and the atomic dipole mode, and deduced that the thermal motion reduces it by approximately 10%. Our findings clarified that the thermal motion is not the limiting factor in light-atom coupling for the observed difference between theory and experiment. The polarization gradient cooling of atoms in dipole traps was investigated as part of the methodology. We showed that the cooling limit in a linearly polarized trap is five times lower than in a circularly polarized trap.

The main experiment of this thesis is the proof-of-principle implementation of 4Pi microscopy as a light-atom interface. The observed 36.6(3)% extinction of a weak coherent field by a single atom is the largest value reported for an atomic emitter in free space. The coupling efficiency was nearly doubled compared to that obtained for one-sided illumination to $\Lambda = 10.1\%$. We further showed that the photon statistics of the transmitted field is modified, which indicates nonlinear light-atom interaction at the single photon level.

A closer look shows that our present system may potentially reach higher coupling up to $\Lambda = 33\%$. The primary limitation of the system is optical aberration, which prevents us from utilising the full aperture of the lenses. Hence, aberration correction has the potential to triple our existing coupling efficiency. Our ongoing effort to perform aberration correction with adaptive optics, in particular, a spatial

light modulator has preliminary results of more than 10% improvement in coupling efficiency.

Our work establishes 4Pi microscopy as an effective technique to couple a propagating light field to an atom. Not only does this contribute towards the development of a distributed quantum network, it leads to exciting prospects to implement effective interactions between photons with tightly focused free-space modes and single atoms. Strongly interacting photons could find application in all-optical quantum information processing [140] and constitute a novel platform to study many-body physics [141, 142]. For example, at $\Lambda = 25\%$, the atom acts as a photon turnstile which converts a coherent field into a single-photon field. While the nonlinearity of the photon-atom interaction observed in this thesis does not reach strongly correlated photons yet, the 4Pi configuration eases the technical requirements of the focusing lens considerably, making the implementation of strong photon-photon interaction feasible. Even stronger interactions up to $\Lambda = 70\%$ are now technically within reach of state-of-the-art objectives in a 4Pi arrangement [143]. The presented approach forms an experimental alternative to cavity/waveguide quantum electrodynamics [19, 35] and Rydberg quantum optics [144, 133, 145, 146].

Appendix A

List of Publications and Conferences

The work presented in this thesis has been published as these articles:

- [Polarization gradient cooling of single atoms in optical dipole traps](#),
Yue Sum Chin, Matthias Steiner, and Christian Kurtsiefer.
Phys. Rev. A. **96**, 033406 (2017).
- [Quantifying the role of thermal motion in free-space light-atom interaction](#),
Yue Sum Chin, Matthias Steiner, and Christian Kurtsiefer.
Phys. Rev. A. **95**, 043809 (2017).
- [Nonlinear photon-atom coupling with 4Pi microscopy](#),
Yue Sum Chin, Matthias Steiner, and Christian Kurtsiefer.
Nat. Commun. **8**, 1200 (2017).

I have presented the results in the following scientific conferences:

- The role of thermal motion in free-space light-atom interaction:
(**Poster**) Okinawa School in Physics 2016: Coherent Quantum Dynamics,
Okinawa, Japan (2016),
(**Talk**) IPS Meeting 2017, Singapore (2017),
(**Talk**) 48th Annual Meeting of the APS Division of Atomic, Molecular and
Optical Physics (DAMOP), Sacramento, CA, USA (2017).
- Strong photon-atom coupling with 4Pi microscopy:
(**Talk**) 3rd International Conference for Young Quantum Information Scien-
tists (YQIS), Erlangen, Germany (2017),
(**Invited Talk**) IPS Meeting 2018, Singapore (2018).

References

- [1] M. Nielsen and I. Chuang, *Quantum Computation and Quantum Information: 10th Anniversary Edition* (Cambridge University Press, 2010).
- [2] P. W. Shor, “Algorithms for quantum computation: discrete logarithms and factoring,” in *Proceedings 35th Annual Symposium on Foundations of Computer Science* (1994) pp. 124–134.
- [3] L. K. Grover, “A fast quantum mechanical algorithm for database search,” in *Proceedings of 28th Annual ACM Symposium on the Theory of Computing* (1996) pp. 212–219.
- [4] L. M. K. Vandersypen, M. Steffen, G. Breyta, C. S. Yannoni, M. H. Sherwood, and I. L. Chuang, “Experimental realization of shor’s quantum factoring algorithm using nuclear magnetic resonance,” *Nature* **414**, 883 (2001).
- [5] B. P. Lanyon, T. J. Weinhold, N. K. Langford, M. Barbieri, D. F. V. James, A. Gilchrist, and A. G. White, “Experimental demonstration of a compiled version of shor’s algorithm with quantum entanglement,” *Phys. Rev. Lett.* **99**, 250505 (2007).
- [6] I. L. Chuang, N. Gershenfeld, and M. Kubinec, “Experimental implementation of fast quantum searching,” *Phys. Rev. Lett.* **80**, 3408 (1998).
- [7] L. DiCarlo, J. M. Chow, J. M. Gambetta, L. S. Bishop, B. R. Johnson, D. I. Schuster, J. Majer, A. Blais, L. Frunzio, S. M. Girvin, and R. J. Schoelkopf, “Demonstration of two-qubit algorithms with a superconducting quantum processor,” *Nature* **460**, 240 (2009).
- [8] S. Boixo, S. V. Isakov, V. N. Smelyanskiy, R. Babbush, N. Ding, Z. Jiang, M. J. Bremner, J. M. Martinis, and H. Neven, “Characterizing quantum supremacy in near-term devices,” *Nat. Phys.* **14**, 595 (2018).
- [9] C. Neill, P. Roushan, K. Kechedzhi, S. Boixo, S. V. Isakov, V. Smelyanskiy, A. Megrant, B. Chiaro, A. Dunsworth, K. Arya, R. Barends, B. Burkett, Y. Chen, Z. Chen, A. Fowler, B. Foxen, M. Giustina, R. Graff, E. Jeffrey, T. Huang, J. Kelly, P. Klimov, E. Lucero, J. Mutus, M. Neeley, C. Quintana, D. Sank, A. Vainsencher, J. Wenner, T. C. White, H. Neven, and J. M. Martinis, “A blueprint for demonstrating quantum supremacy with superconducting qubits,” *Science* **360**, 195 (2018).

References

- [10] M. H. Devoret and R. J. Schoelkopf, “Superconducting circuits for quantum information: An outlook,” *Science* **339**, 1169 (2013).
- [11] D. Barredo, S. de Léséleuc, V. Lienhard, T. Lahaye, and A. Browaeys, “An atom-by-atom assembler of defect-free arbitrary two-dimensional atomic arrays,” *Science* **354**, 1021 (2016).
- [12] M. Endres, H. Bernien, A. Keesling, H. Levine, E. R. Anschuetz, A. Krajenbrink, C. Senko, V. Vuletic, M. Greiner, and M. D. Lukin, “Atom-by-atom assembly of defect-free one-dimensional cold atom arrays,” *Science* **354**, 1024 (2016).
- [13] J. Zhang, G. Pagano, P. W. Hess, A. Kyprianidis, P. Becker, H. Kaplan, A. V. Gorshkov, Z.-X. Gong, and C. Monroe, “Observation of a many-body dynamical phase transition with a 53-qubit quantum simulator,” *Nature* **551**, 601 (2017).
- [14] N. Friis, O. Marty, C. Maier, C. Hempel, M. Holzäpfel, P. Jurcevic, M. B. Plenio, M. Huber, C. Roos, R. Blatt, and B. Lanyon, “Observation of entangled states of a fully controlled 20-qubit system,” *Phys. Rev. X* **8**, 021012 (2018).
- [15] H. J. Kimble, “The quantum internet,” *Nature* **453**, 1023 (2008).
- [16] J. I. Cirac, P. Zoller, H. J. Kimble, and H. Mabuchi, “Quantum state transfer and entanglement distribution among distant nodes in a quantum network,” *Phys. Rev. Lett.* **78**, 3221 (1997).
- [17] J. I. Cirac, A. K. Ekert, S. F. Huelga, and C. Macchiavello, “Distributed quantum computation over noisy channels,” *Phys. Rev. A* **59**, 4249 (1999).
- [18] S. Ritter, C. Nölleke, C. Hahn, A. Reiserer, A. Neuzner, M. Uphoff, M. Mücke, E. Figueroa, J. Bochmann, and G. Rempe, “An elementary quantum network of single atoms in optical cavities,” *Nature* **484**, 195 (2012).
- [19] A. Reiserer and G. Rempe, “Cavity-based quantum networks with single atoms and optical photons,” *Rev. Mod. Phys.* **87**, 1379 (2015).
- [20] N. Sangouard, C. Simon, H. de Riedmatten, and N. Gisin, “Quantum repeaters based on atomic ensembles and linear optics,” *Rev. Mod. Phys.* **83**, 33 (2011).
- [21] M. Saffman, T. G. Walker, and K. Mølmer, “Quantum information with rydberg atoms,” *Rev. Mod. Phys.* **82**, 2313 (2010).
- [22] T. Wilk, A. Gaëtan, C. Evellin, J. Wolters, Y. Miroshnychenko, P. Grangier, and A. Browaeys, “Entanglement of two individual neutral atoms using rydberg blockade,” *Phys. Rev. Lett.* **104**, 010502 (2010).
- [23] L.-M. Duan and C. Monroe, “Colloquium: Quantum networks with trapped ions,” *Rev. Mod. Phys.* **82**, 1209 (2010).

-
- [24] I. V. Inlek, C. Crocker, M. Lichtman, K. Sosnova, and C. Monroe, “Multispecies trapped-ion node for quantum networking,” *Phys. Rev. Lett.* **118**, 250502 (2017).
- [25] A. Delteil, Z. Sun, W.-b. Gao, E. Togan, S. Faelt, and A. Imamoglu, “Generation of heralded entanglement between distant hole spins,” *Nat. Phys.* **12**, 218 (2015).
- [26] A. Reiserer, N. Kalb, M. S. Blok, K. J. M. van Bemmelen, T. H. Taminiau, R. Hanson, D. J. Twitchen, and M. Markham, “Robust quantum-network memory using decoherence-protected subspaces of nuclear spins,” *Phys. Rev. X* **6**, 021040 (2016).
- [27] J. Volz, R. Gehr, G. Dubois, J. Esteve, and J. Reichel, “Measurement of the internal state of a single atom without energy exchange,” *Nature* **475**, 210 (2011).
- [28] A. Reiserer, S. Ritter, and G. Rempe, “Nondestructive detection of an optical photon,” *Science* **342**, 1349 (2013).
- [29] C. Junge, D. O’Shea, J. Volz, and A. Rauschenbeutel, “Strong coupling between single atoms and nontransversal photons,” *Phys. Rev. Lett.* **110**, 213604 (2013).
- [30] C. W. Gardiner, “Inhibition of atomic phase decays by squeezed light: A direct effect of squeezing,” *Phys. Rev. Lett.* **56**, 1917 (1986).
- [31] G. Leuchs and M. Sondermann, “Light-matter interaction in free space,” *J. Mod. Opt.* **60**, 36 (2012).
- [32] E. Vetsch, D. Reitz, G. Sagué, R. Schmidt, S. T. Dawkins, and A. Rauschenbeutel, “Optical interface created by laser-cooled atoms trapped in the evanescent field surrounding an optical nanofiber,” *Phys. Rev. Lett.* **104**, 203603 (2010).
- [33] M. Arcari, I. Söllner, A. Javadi, S. Lindskov Hansen, S. Mahmoodian, J. Liu, H. Thyrestrup, E. H. Lee, J. D. Song, S. Stobbe, and P. Lodahl, “Near-unity coupling efficiency of a quantum emitter to a photonic crystal waveguide,” *Phys. Rev. Lett.* **113**, 093603 (2014).
- [34] P. Lodahl, S. Mahmoodian, and S. Stobbe, “Interfacing single photons and single quantum dots with photonic nanostructures,” *Rev. Mod. Phys.* **87**, 347 (2015).
- [35] M. K. Bhaskar, D. D. Sukachev, A. Sipahigil, R. E. Evans, M. J. Burek, C. T. Nguyen, L. J. Rogers, P. Siyushev, M. H. Metsch, H. Park, F. Jelezko, M. Lončar, and M. D. Lukin, “Quantum nonlinear optics with a germanium-vacancy color center in a nanoscale diamond waveguide,” *Phys. Rev. Lett.* **118**, 223603 (2017).
- [36] S. J. van Enk and H. J. Kimble, “Single atom in free space as a quantum aperture,” *Phys. Rev. A* **61**, 051802 (2000).

References

- [37] S. J. van Enk, “Atoms, dipole waves, and strongly focused light beams,” *Phys. Rev. A* **69**, 043813 (2004).
- [38] M. Sondermann, R. Maiwald, H. Konermann, N. Lindlein, U. Peschel, and G. Leuchs, “Design of a mode converter for efficient light-atom coupling in free space,” *Appl. Phys. B* **89**, 489 (2007).
- [39] M. K. Tey, G. Maslennikov, T. C. H. Liew, S. A. Aljunid, F. Huber, B. Chng, Z. Chen, V. Scarani, and C. Kurtsiefer, “Interfacing light and single atoms with a lens,” *New J. Phys.* **11**, 043011 (2009).
- [40] G. Hétet, L. Slodička, A. Glätzle, M. Hennrich, and R. Blatt, “QED with a spherical mirror,” *Phys. Rev. A* **82**, 063812 (2010).
- [41] A. N. Vamivakas, M. Atatüre, J. Dreiser, S. T. Yilmaz, A. Badolato, A. K. Swan, B. B. Goldberg, A. Imamoğlu, and M. S. Ünlü, “Strong extinction of a far-field laser beam by a single quantum dot,” *Nano Lett.* **7**, 2892 (2007).
- [42] I. Gerhardt, G. Wrigge, P. Bushev, G. Zumofen, M. Agio, R. Pfab, and V. Sandoghdar, “Strong extinction of a laser beam by a single molecule,” *Phys. Rev. Lett.* **98**, 033601 (2007).
- [43] N. Piro, F. Rohde, C. Schuck, M. Almendros, J. Huwer, J. Ghosh, A. Haase, M. Hennrich, F. Dubin, and J. Eschner, “Heralded single-photon absorption by a single atom,” *Nat. Phys.* **7**, 17 (2011).
- [44] A. Maser, B. Gmeiner, T. Utikal, S. Götzinger, and V. Sandoghdar, “Few-photon coherent nonlinear optics with a single molecule,” *Nat. Photonics* **10**, 450 (2016).
- [45] T. H. Tran, P. Siyushev, J. Wrachtrup, and I. Gerhardt, “Extinction of light and coherent scattering by a single nitrogen-vacancy center in diamond,” *Phys. Rev. A* **95**, 053831 (2017).
- [46] M. K. Tey, Z. Chen, S. A. Aljunid, B. Chng, F. Huber, G. Maslennikov, and C. Kurtsiefer, “Strong interaction between light and a single trapped atom without the need for a cavity,” *Nat. Phys.* **4**, 924 (2008).
- [47] V. Leong, M. A. Seidler, M. Steiner, A. Cerè, and C. Kurtsiefer, “Time-resolved scattering of a single photon by a single atom,” *Nat. Commun.* **7**, 13716 (2016).
- [48] E. W. Streed, B. G. Norton, A. Jechow, T. J. Weinhold, and D. Kielpinski, “Imaging of trapped ions with a microfabricated optic for quantum information processing,” *Phys. Rev. Lett.* **106**, 010502 (2011).
- [49] R. Maiwald, A. Golla, M. Fischer, M. Bader, S. Heugel, B. Chalopin, M. Sondermann, and G. Leuchs, “Collecting more than half the fluorescence photons from a single ion,” *Phys. Rev. A* **86**, 043431 (2012).

References

- [50] L. Alber, M. Fischer, M. Bader, K. Mantel, M. Sondermann, and G. Leuchs, “Focusing characteristics of a 4π parabolic mirror light-matter interface,” *J. Eur. Opt. Soc. Rapid Publ.* **13**, 14 (2017).
- [51] M. Fischer, M. Bader, R. Maiwald, A. Golla, M. Sondermann, and G. Leuchs, “Efficient saturation of an ion in free space,” *Appl. Phys. B* **117**, 797 (2014).
- [52] G. R. Guthohrlein, M. Keller, K. Hayasaka, W. Lange, and H. Walther, “A single ion as a nanoscopic probe of an optical field,” *Nature* **414**, 49 (2001).
- [53] S. A. Aljunid, M. K. Tey, B. Chng, T. Liew, G. Maslennikov, V. Scarani, and C. Kurtsiefer, “Phase shift of a weak coherent beam induced by a single atom,” *Phys. Rev. Lett.* **103**, 153601 (2009).
- [54] S. A. Aljunid, B. Chng, J. Lee, M. Paesold, G. Maslennikov, and C. Kurtsiefer, “Interaction of light with a single atom in the strong focusing regime,” *J. Mod. Opt.* **58**, 299 (2011).
- [55] E. Abbe, “Beiträge zur theorie des mikroskops und der mikroskopischen wahrnehmung,” *Arch. Mikroskopische Anat.* **9**, 413 (1873).
- [56] S. Hell and E. H. K. Stelzer, “Properties of a 4π confocal fluorescence microscope,” *J. Opt. Soc. Am. A* **9**, 2159 (1992).
- [57] S. W. Hell, E. H. K. Stelzer, S. Lindek, and C. Cremer, “Confocal microscopy with an increased detection aperture: type-b 4π confocal microscopy,” *Opt. Lett.* **19**, 222 (1994).
- [58] Y.-S. Chin, M. Steiner, and C. Kurtsiefer, “Polarization gradient cooling of single atoms in optical dipole traps,” *Phys. Rev. A* **96**, 033406 (2017).
- [59] Y.-S. Chin, M. Steiner, and C. Kurtsiefer, “Quantifying the role of thermal motion in free-space light-atom interaction,” *Phys. Rev. A* **95**, 043809 (2017).
- [60] Y.-S. Chin, M. Steiner, and C. Kurtsiefer, “Nonlinear photon-atom coupling with 4π microscopy,” *Nat. Commun.* **8**, 1200 (2017).
- [61] M. K. Tey, *Interfacing light and a single quantum system with a lens*, *Ph.D. thesis*, National University of Singapore (2009).
- [62] S. A. Aljunid, *Interaction of a Strongly Focused Light Beam with Single Atoms*, *Ph.D. thesis*, National University of Singapore (2012).
- [63] V. Leong, *Interfacing a Single Atom with Single Photons*, *Ph.D. thesis*, National University of Singapore (2016).
- [64] S. A. Aljunid, G. Maslennikov, Y. Wang, H. L. Dao, V. Scarani, and C. Kurtsiefer, “Excitation of a single atom with exponentially rising light pulses,” *Phys. Rev. Lett.* **111**, 103001 (2013).
- [65] Y. Suzuki and A. Tachibana, “Measurement of the gaussian laser beam divergence,” *Appl. Opt.* **16**, 1481 (1977).

References

- [66] A. H. Firester, M. E. Heller, and P. Sheng, “Knife-edge scanning measurements of subwavelength focused light beams,” *Appl. Opt.* **16**, 1971 (1977).
- [67] S. J. M. Kuppens, K. L. Corwin, K. W. Miller, T. E. Chupp, and C. E. Wieman, “Loading an optical dipole trap,” *Phys. Rev. A* **62**, 013406 (2000).
- [68] S. Bali, K. M. O’Hara, M. E. Gehm, S. R. Granade, and J. E. Thomas, “Quantum-diffractive background gas collisions in atom-trap heating and loss,” *Phys. Rev. A* **60**, R29 (1999).
- [69] H. C. W. Beijerinck, “Rigorous calculation of heating in alkali-metal traps by background gas collisions,” *Phys. Rev. A* **61**, 033606 (2000).
- [70] K. Liu and M. G. Littman, “Novel geometry for single-mode scanning of tunable lasers,” *Opt. Lett.* **6**, 117 (1981).
- [71] A. S. Arnold, J. S. Wilson, and M. G. Boshier, “A simple extended-cavity diode laser,” *Rev. Sci. Instrum.* **69**, 1236 (1998).
- [72] J. H. Shirley, “Modulation transfer processes in optical heterodyne saturation spectroscopy,” *Opt. Lett.* **7**, 537 (1982).
- [73] J. Zhang, D. Wei, C. Xie, and K. Peng, “Characteristics of absorption and dispersion for rubidium d2 lines with the modulation transfer spectrum,” *Opt. Express* **11**, 1338 (2003).
- [74] D. J. McCarron, S. A. King, and S. L. Cornish, “Modulation transfer spectroscopy in atomic rubidium,” *Meas. Sci. Technol.* **19**, 105601 (2008).
- [75] G. C. Bjorklund, “Frequency-modulation spectroscopy: a new method for measuring weak absorptions and dispersions,” *Opt. Lett.* **5**, 15 (1980).
- [76] J. L. Hall, L. Hollberg, T. Baer, and H. G. Robinson, “Optical heterodyne saturation spectroscopy,” *Appl. Phys. Lett.* **39**, 680 (1981).
- [77] H. J. Metcalf and P. van der Straten, *Laser Cooling and Trapping* (Springer, 1999).
- [78] C. J. Foot, *Atomic physics* (Oxford University Press, 2005) pp. 185 – 194.
- [79] D. Steck, “Rubidium 87 d line data,” [http : // steck.us / alkalidata / rubidium87numbers.pdf](http://steck.us/alkalidata/rubidium87numbers.pdf) (2001).
- [80] S. Chu, J. E. Bjorkholm, A. Ashkin, and A. Cable, “Experimental observation of optically trapped atoms,” *Phys. Rev. Lett.* **57**, 314 (1986).
- [81] R. Grimm, M. Weidemüller, and Y. B. Ovchinnikov, “Optical dipole traps for neutral atoms,” *Adv. At. Mol. Opt. Phys.* **42**, 95 (2000).
- [82] N. Schlosser, G. Reymond, I. Protsenko, and P. Grangier, “Sub-poissonian loading of single atoms in a microscopic dipole trap,” *Nature* **411**, 1024 (2001).

References

- [83] N. Schlosser, G. Reymond, and P. Grangier, “Collisional blockade in microscopic optical dipole traps,” *Phys. Rev. Lett.* **89**, 023005 (2002).
- [84] M. S. Safronova and U. I. Safronova, “Critically evaluated theoretical energies, lifetimes, hyperfine constants, and multipole polarizabilities in ^{87}Rb ,” *Phys. Rev. A* **83**, 052508 (2011).
- [85] C.-Y. Shih and M. S. Chapman, “Nondestructive light-shift measurements of single atoms in optical dipole traps,” *Phys. Rev. A* **87**, 063408 (2013).
- [86] L. D. Landau and E. M. Lifshitz, *Mechanics (Third Edition)* (Butterworth-Heinemann, 1976) pp. 80 – 83.
- [87] M. J. Gibbons, C. D. Hamley, C.-Y. Shih, and M. S. Chapman, “Nondestructive fluorescent state detection of single neutral atom qubits,” *Phys. Rev. Lett.* **106**, 133002 (2011).
- [88] A. Fuhrmanek, R. Bourgain, Y. R. P. Sortais, and A. Browaeys, “Free-space lossless state detection of a single trapped atom,” *Phys. Rev. Lett.* **106**, 133003 (2011).
- [89] A. H. Myerson, D. J. Szwer, S. C. Webster, D. T. C. Allcock, M. J. Curtis, G. Imreh, J. A. Sherman, D. N. Stacey, A. M. Steane, and D. M. Lucas, “High-fidelity readout of trapped-ion qubits,” *Phys. Rev. Lett.* **100**, 200502 (2008).
- [90] D. S. Weiss, E. Riis, Y. Shevy, P. J. Ungar, and S. Chu, “Optical molasses and multilevel atoms: experiment,” *J. Opt. Soc. Am. B* **6**, 2072 (1989).
- [91] P. J. Ungar, D. S. Weiss, E. Riis, and S. Chu, “Optical molasses and multilevel atoms: theory,” *J. Opt. Soc. Am. B* **6**, 2058 (1989).
- [92] J. Dalibard and C. Cohen-Tannoudji, “Laser cooling below the doppler limit by polarization gradients: simple theoretical models,” *J. Opt. Soc. Am. B* **6**, 2023 (1989).
- [93] A. M. Kaufman, B. J. Lester, and C. A. Regal, “Cooling a single atom in an optical tweezer to its quantum ground state,” *Phys. Rev. X* **2**, 041014 (2012).
- [94] J. D. Thompson, T. G. Tiecke, A. S. Zibrov, V. Vuletić, and M. D. Lukin, “Coherence and raman sideband cooling of a single atom in an optical tweezer,” *Phys. Rev. Lett.* **110**, 133001 (2013).
- [95] P. Sompet, Y. H. Fung, E. Schwartz, M. D. J. Hunter, J. Phrompao, and M. F. Andersen, “Zeeman-insensitive cooling of a single atom to its two-dimensional motional ground state in tightly focused optical tweezers,” *Phys. Rev. A* **95**, 031403 (2017).
- [96] W. Rosenfeld, F. Hocke, F. Henkel, M. Krug, J. Volz, M. Weber, and H. Weinfurter, “Towards long-distance atom-photon entanglement,” *Phys. Rev. Lett.* **101**, 260403 (2008).

References

- [97] C. Tuchendler, A. M. Lance, A. Browaeys, Y. R. P. Sortais, and P. Grangier, “Energy distribution and cooling of a single atom in an optical tweezer,” *Phys. Rev. A* **78**, 033425 (2008).
- [98] S.-Q. Shang, B. Sheehy, P. van der Straten, and H. Metcalf, “Velocity-selective magnetic-resonance laser cooling,” *Phys. Rev. Lett.* **65**, 317 (1990).
- [99] S.-Q. Shang, B. Sheehy, H. Metcalf, P. van der Straten, and G. Nienhuis, “Velocity-selective resonances and sub-doppler laser cooling,” *Phys. Rev. Lett.* **67**, 1094 (1991).
- [100] M. Walhout, J. Dalibard, S. L. Rolston, and W. D. Phillips, “ $\sigma_+ - \sigma_-$ optical molasses in a longitudinal magnetic field,” *J. Opt. Soc. Am. B* **9**, 1997 (1992).
- [101] M. Walhout, U. Sterr, and S. L. Rolston, “Magnetic inhibition of polarization-gradient laser cooling in $\sigma_+ - \sigma_-$ optical molasses,” *Phys. Rev. A* **54**, 2275 (1996).
- [102] J. Werner, H. Wallis, and W. Ertmer, “Atoms with anomalous zeeman effect in a 1d-magneto-optical molasses,” *Opt. Commun.* **94**, 525 (1992).
- [103] S. Chang, T. Y. Kwon, H. S. Lee, and V. G. Minogin, “Laser sub-doppler cooling of atoms in an arbitrarily directed magnetic field,” *Phys. Rev. A* **66**, 043404 (2002).
- [104] I. H. Deutsch and P. S. Jessen, “Quantum-state control in optical lattices,” *Phys. Rev. A* **57**, 1972 (1998).
- [105] K. L. Corwin, S. J. M. Kuppens, D. Cho, and C. E. Wieman, “Spin-polarized atoms in a circularly polarized optical dipole trap,” *Phys. Rev. Lett.* **83**, 1311 (1999).
- [106] F. Le Kien, P. Schneeweiss, and A. Rauschenbeutel, “Dynamical polarizability of atoms in arbitrary light fields: general theory and application to cesium,” *Eur. Phys. J. D* **67**, 92 (2013).
- [107] C. Cohen-Tannoudji and J. Dupont-Roc, “Experimental study of zeeman light shifts in weak magnetic fields,” *Phys. Rev. A* **5**, 968 (1972).
- [108] V. Minogin and O. Serimaa, “Resonant light pressure forces in a strong standing laser wave,” *Opt. Commun.* **30**, 373 (1979).
- [109] J. Lee, J. A. Grover, L. A. Orozco, and S. L. Rolston, “Sub-doppler cooling of neutral atoms in a grating magneto-optical trap,” *J. Opt. Soc. Am. B* **30**, 2869 (2013).
- [110] S. M. Tan, “A computational toolbox for quantum and atomic optics,” *J. Opt. B* **1**, 424 (1999).
- [111] S. M. Tan, “A quantum optics toolbox for Matlab,” <http://qo.phy.auckland.ac.nz/toolbox/> (2002).

References

- [112] B. Richards and E. Wolf, “Electromagnetic diffraction in optical systems. ii. structure of the image field in an aplanatic system,” *Proc. R. Soc. London, Ser. A* **253**, 358 (1959).
- [113] C. Salomon, J. Dalibard, W. D. Phillips, A. Clairon, and S. Guellati, “Laser cooling of cesium atoms below $3 \mu\text{k}$,” *Europhys. Lett.* **12**, 683 (1990).
- [114] C. Gerz, T. W. Hodapp, P. Jessen, K. M. Jones, W. D. Phillips, C. I. Westbrook, and K. Molmer, “The temperature of optical molasses for two different atomic angular momenta,” *Europhys. Lett.* **21**, 661 (1993).
- [115] D. J. Wineland, J. Dalibard, and C. Cohen-Tannoudji, “Sisyphus cooling of a bound atom,” *J. Opt. Soc. Am. B* **9**, 32 (1992).
- [116] J. I. Cirac, R. Blatt, A. S. Parkins, and P. Zoller, “Laser cooling of trapped ions with polarization gradients,” *Phys. Rev. A* **48**, 1434 (1993).
- [117] S. Ejtemaee and P. C. Haljan, “3d sisyphus cooling of trapped ions,” *Phys. Rev. Lett.* **119**, 043001 (2017).
- [118] L. Slodička, G. Hétet, S. Gerber, M. Hennrich, and R. Blatt, “Electromagnetically induced transparency from a single atom in free space,” *Phys. Rev. Lett.* **105**, 153604 (2010).
- [119] L. Slodička, G. Hétet, M. Hennrich, and R. Blatt, “Free space interference experiments with single photons and single ions,” in *Engineering the Atom-Photon Interaction: Controlling Fundamental Processes with Photons, Atoms and Solids*, edited by A. Predojević and M. W. Mitchell (Springer International Publishing, Cham, 2015) pp. 99–124.
- [120] G. Zumofen, N. M. Mojarad, V. Sandoghdar, and M. Agio, “Perfect reflection of light by an oscillating dipole,” *Phys. Rev. Lett.* **101**, 180404 (2008).
- [121] D. Hucul, I. V. Inlek, G. Vittorini, C. Crocker, S. Debnath, S. M. Clark, and C. Monroe, “Modular entanglement of atomic qubits using photons and phonons,” *Nat. Phys.* **11**, 37 (2014).
- [122] M. Ghadimi, V. Blūms, B. G. Norton, P. M. Fisher, S. C. Connell, J. M. Amini, C. Volin, H. Hayden, C.-S. Pai, D. Kielpinski, M. Lobino, and E. W. Streed, “Scalable ion-photon quantum interface based on integrated diffractive mirrors,” *npj Quantum Inf.* **3**, 4 (2017).
- [123] C. Teo and V. Scarani, “Lenses as an atom–photon interface: A semiclassical model,” *Opt. Commun.* **284**, 4485 (2011).
- [124] M. Sondermann and G. Leuchs, “Photon-atom coupling with parabolic mirrors,” in *Engineering the Atom-Photon Interaction: Controlling Fundamental Processes with Photons, Atoms and Solids*, edited by A. Predojević and M. W. Mitchell (Springer International Publishing, Cham, 2015) pp. 75–98.

References

- [125] J.-T. Shen and S. Fan, “Strongly correlated two-photon transport in a one-dimensional waveguide coupled to a two-level system,” *Phys. Rev. Lett.* **98**, 153003 (2007).
- [126] T. G. Tiecke, J. D. Thompson, N. P. de Leon, L. R. Liu, V. Vuletic, and M. D. Lukin, “Nanophotonic quantum phase switch with a single atom,” *Nature* **508**, 241 (2014).
- [127] I. Shomroni, S. Rosenblum, Y. Lovsky, O. Bechler, G. Guendelman, and B. Dayan, “All-optical routing of single photons by a one-atom switch controlled by a single photon,” *Science* **345**, 903 (2014).
- [128] B. Hacker, S. Welte, G. Rempe, and S. Ritter, “A photon-photon quantum gate based on a single atom in an optical resonator,” *Nature* **536**, 193 (2016).
- [129] K. M. Birnbaum, A. Boca, R. Miller, A. D. Boozer, T. E. Northup, and H. J. Kimble, “Photon blockade in an optical cavity with one trapped atom,” *Nature* **436**, 87 (2005).
- [130] B. Dayan, A. S. Parkins, T. Aoki, E. P. Ostby, K. J. Vahala, and H. J. Kimble, “A photon turnstile dynamically regulated by one atom,” *Science* **319**, 1062 (2008).
- [131] A. Reinhard, T. Volz, M. Winger, A. Badolato, K. J. Hennessy, E. L. Hu, and A. Imamoglu, “Strongly correlated photons on a chip,” *Nat. Photonics* **6**, 93 (2012).
- [132] I.-C. Hoi, T. Palomaki, J. Lindkvist, G. Johansson, P. Delsing, and C. M. Wilson, “Generation of nonclassical microwave states using an artificial atom in 1d open space,” *Phys. Rev. Lett.* **108**, 263601 (2012).
- [133] T. Peyronel, O. Firstenberg, Q.-Y. Liang, S. Hofferberth, A. V. Gorshkov, T. Pohl, M. D. Lukin, and V. Vuletic, “Quantum nonlinear optics with single photons enabled by strongly interacting atoms,” *Nature* **488**, 57 (2012).
- [134] D. E. Chang, A. S. Sorensen, E. A. Demler, and M. D. Lukin, “A single-photon transistor using nanoscale surface plasmons,” *Nat. Phys.* **3**, 807 (2007).
- [135] H. Zheng, D. J. Gauthier, and H. U. Baranger, “Waveguide qed: Many-body bound-state effects in coherent and fock-state scattering from a two-level system,” *Phys. Rev. A* **82**, 063816 (2010).
- [136] R. H. Brown and R. Q. Twiss, “Correlation between photons in two coherent beams of light,” *Nature* **177**, 27 (1956).
- [137] Reynaud, Serge, “Resonance fluorescence : the dressed atom approach,” *Ann. Phys.* **8**, 315 (1983).
- [138] V. Gomer, B. Ueberholz, S. Knappe, F. Strauch, D. Frese, and D. Meschede, “Decoding the dynamics of a single trapped atom from photon correlations,” *Appl. Phys. B* **67**, 689 (1998).

References

- [139] M. Weber, J. Volz, K. Saucke, C. Kurtsiefer, and H. Weinfurter, “Analysis of a single-atom dipole trap,” *Phys. Rev. A* **73**, 043406 (2006).
- [140] D. E. Chang, V. Vuletic, and M. D. Lukin, “Quantum nonlinear optics — photon by photon,” *Nat. Photonics* **8**, 685 (2014).
- [141] D. E. Chang, V. Gritsev, G. Morigi, V. Vuletic, M. D. Lukin, and E. A. Demler, “Crystallization of strongly interacting photons in a nonlinear optical fibre,” *Nat. Phys.* **4**, 884 (2008).
- [142] M. Girardeau, “Relationship between systems of impenetrable bosons and fermions in one dimension,” *Journal of Mathematical Physics* **1**, 516 (1960).
- [143] C. Robens, S. Brakhane, W. Alt, F. Kleiβler, D. Meschede, G. Moon, G. Ramola, and A. Alberti, “High numerical aperture ($na = 0.92$) objective lens for imaging and addressing of cold atoms,” *Opt. Lett.* **42**, 1043 (2017).
- [144] J. D. Pritchard, D. Maxwell, A. Gauguet, K. J. Weatherill, M. P. A. Jones, and C. S. Adams, “Cooperative atom-light interaction in a blockaded rydberg ensemble,” *Phys. Rev. Lett.* **105**, 193603 (2010).
- [145] O. Firstenberg, C. S. Adams, and S. Hofferberth, “Nonlinear quantum optics mediated by rydberg interactions,” *J. Phys. B* **49**, 152003 (2016).
- [146] A. Paris-Mandoki, C. Braun, J. Kumlin, C. Tresp, I. Mirgorodskiy, F. Christaller, H. P. Büchler, and S. Hofferberth, “Free-space quantum electrodynamics with a single rydberg superatom,” *Phys. Rev. X* **7**, 041010 (2017).